RSC Advances

PAPER

View Article Online
View Journal | View Issue

Cite this: *RSC Adv.*, 2025, **15**, 20916

Enhanced corrosion resistance of zinc phosphate coatings on mild steel through incorporation of nanocrystalline CeO_2 and CeO_2–CuO nanocomposite†

S. Ayesha Barsana,[a] A. Sultan Nasar [b] and M. J. Umapathy *[a]

Herein, 5–10 nm-sized rod-like nanocrystalline CeO_2 and CeO_2–CuO nanocomposite were synthesized and incorporated into zinc phosphate coatings as corrosion inhibition additives. The formulated coatings were studied thoroughly on mild steel in 3.5% NaCl solution and compared with unmodified coating. The concentration of the additive was varied from 0.3 g L^{-1} to 0.9 g L^{-1} with three step-ups. X-ray and surface analysis results revealed that both additives favoured the formation of more compact coatings with densely packed zinc phosphate crystals and reduced iron content. Compared with the unmodified coating, the metal oxide incorporated coatings showed low corrosion current density (I_{corr}) and corrosion rate and high polarisation resistance (R_p) and charge transfer resistance (R_{ct}), confirming that these nanomaterials act as corrosion inhibitors. Among the three concentrations used, nanocrystalline CeO_2 performed well at 0.6 g L^{-1} and CeO_2–CuO nanocomposite performed well even at low concentration of 0.3 g L^{-1}, with a more than fifty-one times lower corrosion rate and twenty times higher polarisation resistance (R_p) compared with unmodified coating. Nanocrystalline CeO_2 increased the R_{ct} from 114 Ω cm^2 to 427.5 Ω cm^2 at 0.6 g L^{-1}, whereas the CeO_2–CuO nanocomposite increased this value up to 3645 Ω cm^2 at 0.3 g L^{-1}. Enhanced corrosion resistance of these coatings was confirmed with an accelerated salt-spray test.

Received 22nd April 2025
Accepted 5th June 2025

DOI: 10.1039/d5ra02800k

rsc.li/rsc-advances

1. Introduction

Low carbon steel, commonly known as mild steel in which the carbon content normally varies from 0.05 to 0.3 weight percentage, is known for its high ductility, machinability and weldability. In addition to these properties, its cost-effectiveness makes it a highly sought-after material for many large and small fabrications, notably automobile parts such as body panels, camshaft, shaft axles, engine cylinders and bolts, gears, brackets, pins and washers. This alloy is more susceptible to rusting when exposed to moisture, which deteriorates the metal's performance, leading to random failures.[1] Despite this drawback, mild steel remains an ideal choice for applications where high tensile strength and durability are required.

Preventive measures such as using corrosion inhibitors and applying protective coatings can help mitigate these failures.[2–5] Coatings are one of the smart ways to control corrosion. Phosphate conversion coatings—particularly zinc phosphate conversion coatings—are more advantageous over other coating methods.[6–8] This coating protects the surface of the steel against corrosion by forming a thin, non-conducting layer of insoluble phosphates.[9] Zinc phosphate coatings can be applied to a variety of materials, including high carbon steel, medium carbon steel,[10] low carbon steel,[11] galvanized steel,[12] magnesium alloy,[13] and aluminum alloy.[14] Owing to the ease of application, efficiency and compatibility with various substrates, this coating emerged as a preferred choice for many industrial applications.[15]

However, the corrosion resistance of the phosphate coatings in adverse environments is often limited due to open pores and cracks through which the electrolytes diffuse and react with the underlying steel surface and induce the conversion of iron into iron oxides and hydroxides.[16,17] Many additives improve the coating performance. Careful selection and infusion of these additives are vital for achieving desired coating characteristics, such as improved corrosion resistance, adhesion, hardness, and overall durability of the coated metal surface.

In the recent past, the use of nanomaterials as corrosion inhibitors gained significant attention. The presence of nanomaterials in the coating composition control the electrochemical process that occurs at the interface of the coating and the metal surface. Metal oxides like SiO_2,[18] ZrO_2,[19] TiO_2,[20] and

[a]*Department of Chemistry, Anna University, College of Engineering, Guindy, Chennai 600025, India. E-mail: mj_umapathy@yahoo.co.in*

[b]*Department of Polymer Science, University of Madras, Guindy Campus, Chennai 600025, India*

† Electronic supplementary information (ESI) available. See DOI: https://doi.org/10.1039/d5ra02800k

Al_2O_3 (ref. 21) in the nanoscale, nanocomposites like Al_2O_3/Mo[22] and two-dimensional nanosheets like graphene oxide[23,24] and boron nitride[25] were studied as additives for zinc phosphate coatings and the results were promising. Their unique properties such as high surface area, water repellent nature, antioxidant properties, and barrier functions against aggressive agents collectively improve the performance of the coatings.[26] They also speed-up the phosphate treatment process at room temperature, and thus reduce energy consumption.

Bagal and co-workers found that the corrosion rate significantly reduced from 8 mpy to 3.5 mpy, and the coating porosity decreased by 50% upon incorporation of TiO_2 in the phosphate coating.[20] In another report, Young Zhou and co-workers explored the effect of the addition of nano CeO_2 into zinc phosphate coatings applied on magnesium alloy AZ91D and showed improved adhesion and micro-hardness of the coating at a concentration of 2 g L^{-1}.[27] Riyas and co-workers reported Al_2O_3/Mo composite incorporated zinc phosphate coatings for galvanised steel.[22] They found that the Al_2O_3/Mo particles acted as nucleating agents, forming highly compact and dense phosphate crystals. Moreover, the resulting coating showed high charge-transfer resistance and improved corrosion resistance. Deepa and co-workers formulated zinc coatings with $BiVO_4/TiO_2$ composites.[28] This coating achieved a water contact angle of 120.2°, which improved its self-cleaning properties. Additionally, it demonstrated a high inhibition efficiency of 91.68% and great corrosion resistance. These recent findings recognise metal oxides as anti-corrosion additives for coatings.

The present study focuses on abundant rare earth metal oxide nanoparticle, *i.e.*, nano CeO_2 and its nanocomposite with CuO as additives for zinc phosphate coatings. Generally, this class of metal oxides enhances microstructure formation, refines grain boundaries, and improves overall durability of the coating.[29] Rare earth elements inhibit corrosion by forming an insoluble film of oxides and hydroxides, which replaces the natural oxide film on metal surfaces.[30] Among the various rare earth elements, cerium with high oxidation state (Ce^{3+} and Ce^{4+}) forms stable oxides that provide barrier protection against corrosion.[31] As far as copper is concerned, it has good thermal stability, mechanical workability and acts as like a noble metal in stringent environmental conditions. A nano copper oxide coating on the same metal formed by anodization was found to increase the corrosion protection efficiency by 86.2% in 3.5% NaCl and 74.5% in 2 mg per L NH_3.[32] The insoluble nature of copper in water increases the hydrophobicity of the coating.[33] We aimed to develop new zinc phosphate conversion coatings using nanocrystalline CeO_2 and CeO_2–CuO nanocomposite as corrosion inhibition additives. Accordingly, some zinc phosphate conversion coatings were formulated and applied on mild steel. Herein, the synthesis of nanoadditives was reported and the anti-corrosion performance of the coatings was impressive.

2. Materials and methods

2.1 Materials

Analytical grade cerous nitrate hexahydrate ($Ce(NO_3)_3 \cdot 6H_2O$, CAS number 10294-41-4), cupric nitrate trihydrate ($Cu(NO_3)_2 \cdot 3H_2O$, CAS 10031-43-3), zinc oxide (ZnO, CAS number 1314-13-2), orthophosphoric acid (85% phosphoric acid (H_3PO_4), CAS number 7664-38-2), sodium hydroxide, sodium carbonate, sodium nitrite and sodium chloride were purchased from Sisco Research Laboratories Pvt. Ltd and used without further purification. Mild steel of grade IS 513/2008 GR4 was purchased from the local market and its chemical composition was given in Table S1 (ESI).† All the experiments were carried out in distilled water.

2.2 Synthesis of CeO_2 nanoparticle

CeO_2 in the form of nanoparticle was prepared from cerium nitrate hexahydrate ($Ce(NO_3)_3 \cdot 6H_2O$) and sodium carbonate (Na_2CO_3) by the precipitation method. A 0.2 M solution of cerium nitrate hexahydrate was prepared by dissolving 4.34 g of $Ce(NO_3)_3 \cdot 6H_2O$ in 50 mL of distilled water and the solution was subjected to continuous stirring. To this, a 1 M sodium carbonate solution was added dropwise until the pH of the solution reached 10. The whole mixture was stirred for a further 60 minutes, resulting in a pale, yellow coloured liquid–solid suspension. This suspension was centrifuged at 2000 rpm, filtered and washed with deionized water several times to remove the impurities. The obtained precipitate was first dried in a vacuum oven maintained at 80 °C, milled to obtain a fine powder and subsequently calcined at 450 °C in the presence of air for 3 h to obtain CeO_2 as a nanopowder.

2.3 Preparation of CeO_2–CuO nanocomposite

CeO_2–CuO nanocomposite was prepared *via* the co-precipitation method. Twenty-five mL of 0.2 M solutions of $Ce(NO_3)_3 \cdot 6H_2O$ and $Cu(NO_3)_2 \cdot 3H_2O$ were mixed together and stirred for 1 h. Next, a 1 M sodium hydroxide solution was added dropwise to the solution until the pH of the solution attained 10. Then, the whole mixture was stirred for 60 min to obtain a pale blue coloured liquid–solid suspension. The rest of the procedure employed to obtain CeO_2–CuO nanocomposite was similar to that adopted for the preceding synthesis.

2.4 Characterizations of CeO_2 nanoparticle and CeO_2–CuO nanocomposite

The functional groups of the synthesised metal oxide and composite were analysed using a Thermo iS50 Fourier-transform infra-red spectrophotometer (FT-IR) in the mid IR range of 400–4000 cm^{-1}; samples were prepared using the KBr pellet method. The morphology and elemental distribution of the prepared CeO_2 nanoparticle and CeO_2–CuO nanocomposite were examined by field emission scanning electron microscopy (FE-SEM) combined with energy dispersive X-ray spectroscopy (EDAX) (TESCAN VEGA3 model and Carl Zeiss Sigma 300 model instruments). The phase and crystalline characteristics of the prepared CeO_2 and CeO_2–CuO composite were studied using a powder X-ray diffraction (XRD) technique with an Empyrean Series III Diffractometer operated with a monochromatic Cu Kα radiation source ($\lambda = 0.15418$ nm). The samples were examined between 2θ of 20° and 90° with a 0.05° step-up and 0.02 s per

step. The crystallite size was calculated using the Debye–Scherrer formula as given in eqn (1).

$$D = K\lambda/\beta\cos\theta \quad (1)$$

where D represents the average crystallite size, K is a dimensionless shape factor (0.98), λ is the X-ray wavelength, θ is the diffraction angle and β is the full width at half maximum of the diffraction peak in radians. The elemental compositions of the prepared nanomaterials were analysed using X-ray photoelectron spectroscopy (XPS) (Thermo Fisher, model K-Alpha-KAN9954133) using monochromatic Al-Kα radiation at 150 W with an X-ray power gun at room temperature. The thermal stability of the nanoparticle and nanocomposite were determined by thermogravimetry (TG) and differential thermal analyses (DTA). These experiments were performed with a simultaneous thermal analyser (Shimadzu, DTG 60 Series) under a nitrogen atmosphere at a 100 mL per min gas flow rate. The temperature was varied from 30 °C to 700 °C and the heating rate was set at 10 °C min^{-1}.

2.5 Preparation of phosphating bath

First, the phosphating bath solution was partially prepared by mixing 7 g of zinc oxide (ZnO) in 14 mL of 85% ortho phosphoric acid (H_3PO_4). Stirring the obtained paste like mass with 50 mL of distilled water in a magnetic stirrer for 30 min resulted in a clear solution. Then, this solution was diluted to 1 litre with distilled water. The quantity of zinc oxide and orthophosphoric acid was fixed after several trial experiments. Appropriate quantities of the remaining ingredients were added to this partial solution immediately prior to experiments to make a complete formulation. The chemical composition of the zinc phosphating bath is given in Table 1.

The conventional zinc phosphate coating composition was modified by the addition of synthesized CeO_2 nanoparticle and CeO_2–CuO nanocomposite into the phosphating bath. Based on the quantity of the additive added (0.3 g, 0.6 g or 0.9 g) into the zinc phosphating bath, the obtained coatings were named as (i) ZnP-0.3CO, ZnP-0.6CO, ZnP-0.9CO, respectively for cerium oxide and (ii) ZnP-0.3COCO, ZnP-0.6COCO, ZnP-0.9COCO, respectively for cerium oxide–copper oxide composite. The zinc phosphate coating formulated without the synthesised nanomaterials as additive is simply represented as ZnP in this study.

Table 1 Chemical composition of zinc phosphating bath

Ingredient	Quantity
ZnO	7 g L^{-1}
Phosphoric acid	14 mL L^{-1}
Sodium nitrite	1 g L^{-1}
Nanocrystalline CeO_2[a]	0.3 g L^{-1} (or), 0.6 g L^{-1} (or), 0.9 g L^{-1}
CeO_2–CuO nanocomposite[a]	0.3 g L^{-1} (or), 0.6 g L^{-1} (or), 0.9 g L^{-1}
Total acid	28.2 (Points)
Free acid	2.9 (Points)
TA : FA	9.7 : 1
pH	2.8

[a] Either CeO_2 or CeO_2–CuO was used for a formulation.

2.6 Determination of free acid and total acid

To obtain quality coatings, bath parameters such as total acid value (TA), free acid value (FA) and their ratio should be maintained at appropriate levels. These values were calculated by titration of the bath solution against 0.1 N NaOH. The total acid value was determined by titrating 10 mL of the bath solution against 0.1 N NaOH using phenolphthalein as indicator. The end-point was colour change of the bath solution from colourless to pink (1 mL = 1 point). The free acid value was determined by following the same procedure using methyl orange as indicator. Here, the end-point was a colour change of the bath solution from orange to yellow. In general, the total acid value is maintained between 10 and 25 (points) and the free acid value is maintained between 0.5 and 3 (points) to obtain optimal coatings. The ratio of free acid to total acid gives the acid coefficient of the bath; the higher the acid co-efficient value, the better the coating produced. The total acid value, free acid value and the acid coefficient of the phosphating bath are given in Table 1.

2.7 Preparation of substrate and phosphate treatment

Steel panels were fabricated to a dimension of 20 mm × 20 mm × 0.8 mm. The residual rust and scales on the steel surface were removed by abrading them with SiC papers differing in grit number and washed with distilled water. Contaminants like dirt, oil and grease were removed by soaking the panel in 10% NaOH solution at room temperature for 30 min and washed with excess distilled water followed by rinsing with acetone. The cleaned steel substrates were immersed in a zinc phosphating bath at room temperature for 30 min with the composition given in Table 1. After this surface treatment, the panels were dried in air and kept in a desiccator for further studies.

2.8 Characterizations of zinc phosphate coatings

2.8.1 Evaluation of corrosion resistance of CeO_2 nanoparticle and CeO_2–CuO nanocomposite incorporated zinc phosphate coating. The corrosion protection properties of the phosphate coated steel panels were studied in 3.5 wt% NaCl aqueous solution employing an electrochemical work station (CH Instruments Model 1130A). The electrochemical analyses were performed with a three-electrode cell system; the developed coating with an exposed area of 1 cm^2 was used as a working electrode, calomel electrode was used as reference electrode and platinum electrode was used as a counter electrode. The coatings were immersed in NaCl solution for 30 min before commencing the analysis to achieve a stable open circuit potential. The potentiodynamic polarisation curves were plotted to determine the corrosion current density (I_{corr}) and corrosion potential (E_{corr}). The polarisation resistance (R_p) was calculated using the Stern–Geary eqn (2).

$$R_p = \frac{\beta_a \times \beta_c}{2.3 i_{corr}(\beta_a + \beta_c)} \quad (2)$$

where β_a, β_c and I_{corr} are the anodic Tafel slope, cathodic Tafel slope and corrosion current density, respectively. The corrosion rate in mm per year was calculated using eqn (3).

$$CR = K\frac{i_{corr}}{\rho}EW \quad (3)$$

where K (3.27×10^{-3}) is the unit conversion factor, I_{corr} is the corrosion current density in μA cm^{-2}, ρ is the density of the metal in g cm^{-3} and EW is the equivalent weight of the metal (considered dimensionless).

The data obtained from the electrochemical impedance spectroscopy were presented as Nyquist and Bode plots. Bode

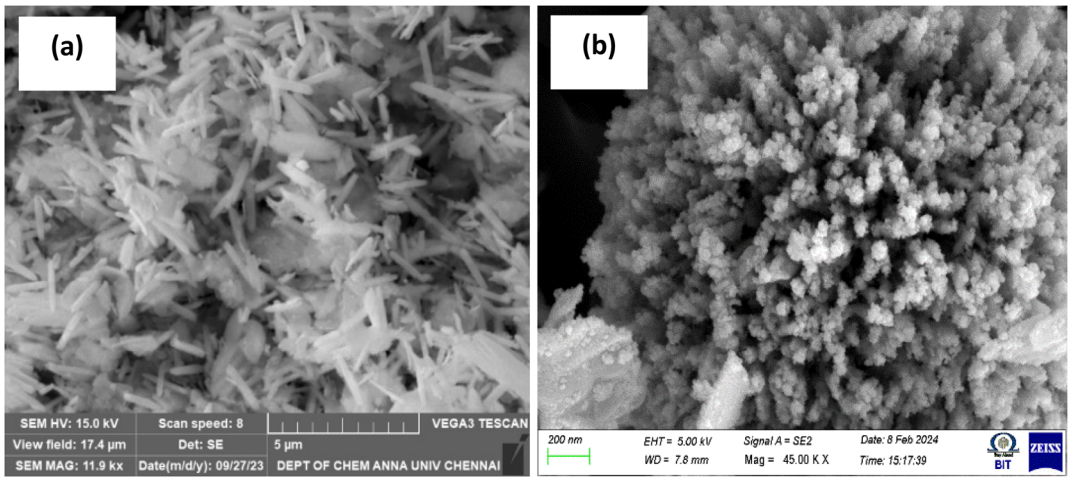

Fig. 1 SEM micrograph of (a) nanocrystalline CeO_2 (scale bar = 5 μm) and (b) CeO_2–CuO nanocomposite (scale bar = 200 nm).

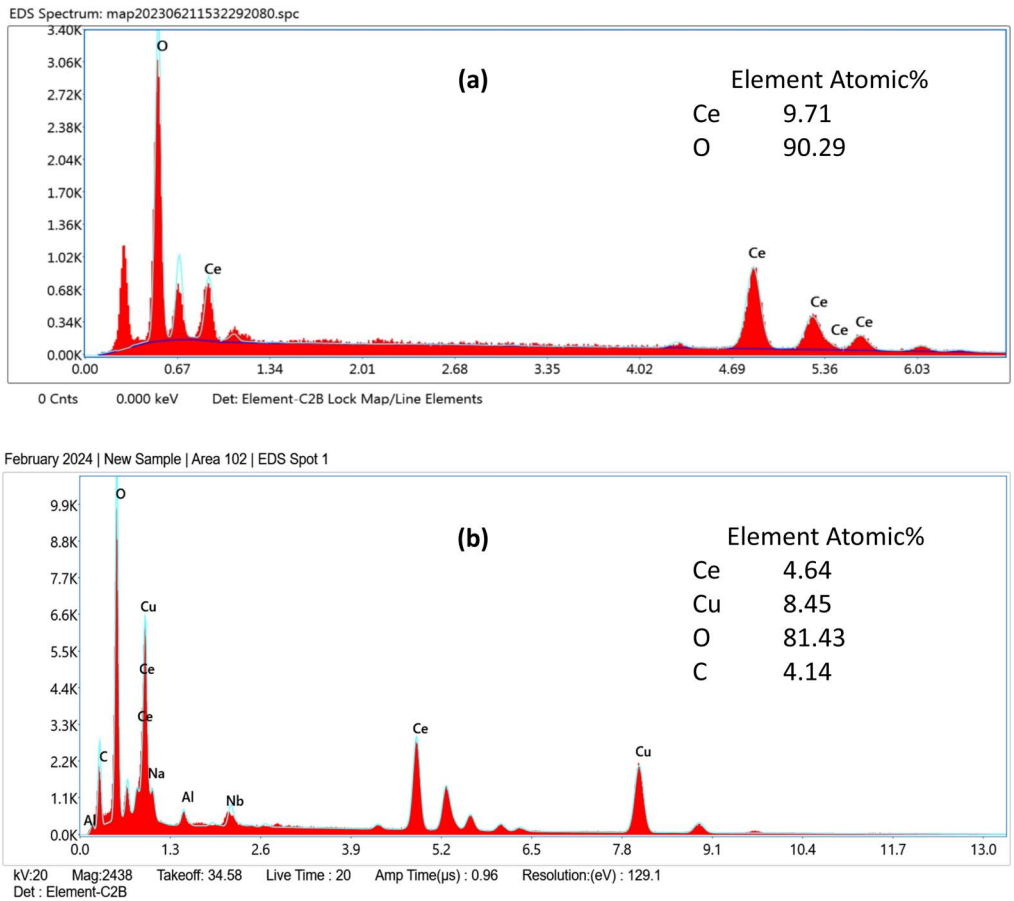

Fig. 2 EDAX spectrum of (a) nanocrystalline CeO_2 and (b) CeO_2–CuO nanocomposite.

impedance and the phase angle were plotted as $\log|Z|$ *vs.* $\log(f)$ and −phase angle *vs.* $\log(f)$, where $|Z|$ represents the absolute impedance and f indicates the frequency. The obtained data were fitted using ZSimpWin software (Princeton Applied Research, USA) to obtain an appropriate equivalent circuit.

2.8.2 Salt-spray test. The coated samples (panels) were subjected to a neutral salt spray test. These tests were performed in a closed chamber, where a 5% sodium chloride solution was atomized into a fine mist and sprayed over the coatings. This salt fog simulates a corrosive environment in accordance with the ASTM B117 standard. After completion of 48 hours of spray time, the corrosion resistance of the coatings was recorded through photographs of rust formed and evaluated. From the coating's weight noted before and after the test, the corrosion rate was calculated using eqn (4).

$$\text{Corrosion rate} = 534W/DAT \quad (4)$$

where W = weight loss in grams; D = density of the metal in g cm^{-3}; A = exposed area of the sample in cm^2; T = time of exposure in hours and the numerical value; 534 is a conversion factor for g cm^{-2} to mpy units.

The percentage inhibition efficiency 'P' of the additives was calculated from the following relationship:

$$P = 100[\text{CR}_{\text{uninhibited}} - \text{CR}_{\text{inhibited}}/\text{CR}_{\text{uninhibited}}] \quad (5)$$

where $\text{CR}_{\text{uninhibited}}$ and $\text{CR}_{\text{inhibited}}$ are the corrosion rates of the coating without and with additive (*i.e.*, CeO_2 nanoparticle or CeO_2–CuO nanocomposite), respectively.

Other characterizations of the coatings were described in the ESI section,† including the analysis of functional groups, surface morphology, elemental and phase composition, measurements of surface wetting, coating weight, hardness and adhesion tests.

3. Results and discussion

3.1 Synthesis of nano CeO_2 and CeO_2–CuO nanocomposite

Cerium oxide nanoparticles and its composite with copper oxide were synthesized *via* an economically simple-cum-attractive precipitation method as described in Fig. S1 and S2, respectively (ESI).† For both the synthesis, the respective hydrous forms of metal nitrates were used as precursors with sodium carbonate and sodium hydroxide used as precipitating agents. The reactions were carried out in water medium at pH = 10 and subsequent physical processes of fine grinding and calcination carried out at 450 °C yielded pale yellow CeO_2 and greyish black CeO_2–CuO nanoparticles. The yield of the compound was quantitative, *i.e.*, >80%. It is worth mentioning that the amount of obtained CeO_2 was considerably higher than the expected theoretical value, indicating that this material was in hydrated form.[34,35]

3.2 Characterisation of prepared nanoadditives

3.2.1 Formation, morphology and composition of nano CeO_2 and CeO_2–CuO nanocomposite. The FT-IR spectra of nano CeO_2 and CeO_2–CuO nanocomposite were essentially identical and were shown in Fig. S3 (ESI).† They exhibited a peak for fundamental stretching of metal–oxygen bonds in the expected finger-print region at around 500 cm^{-1}, confirming the formation of metal oxides from the metal nitrate precursors. The broad and strong absorption peak at 3433 cm^{-1} and a strong absorption band at 1384 cm^{-1} was due to moisture adsorbed on the surface of the compounds. This suggests that these nanomaterials are porous in nature. The peaks at 1572 cm^{-1} and 1384 cm^{-1} are respectively due to the anti and sym stretching vibration of the N–O group of residual nitrate reagents present in the compounds. A weak band at 1059 cm^{-1} is due to atmospheric carbon dioxide absorbed by the compounds during the storage and analysis.[35–38]

The surface morphology and nano-scale structure of CeO_2 and CeO_2–CuO composite were examined through FE-SEM and the vivid pictures are shown in Fig. 1. The SEM images reveal that the CeO_2 crystals possess small rod-like structures that grew randomly in all directions with an even surface.[39] On the other hand, the CeO_2–CuO composite grew perpendicularly with an uneven surface and showed a bamboo stem like structure. This well-defined surface morphology is an important

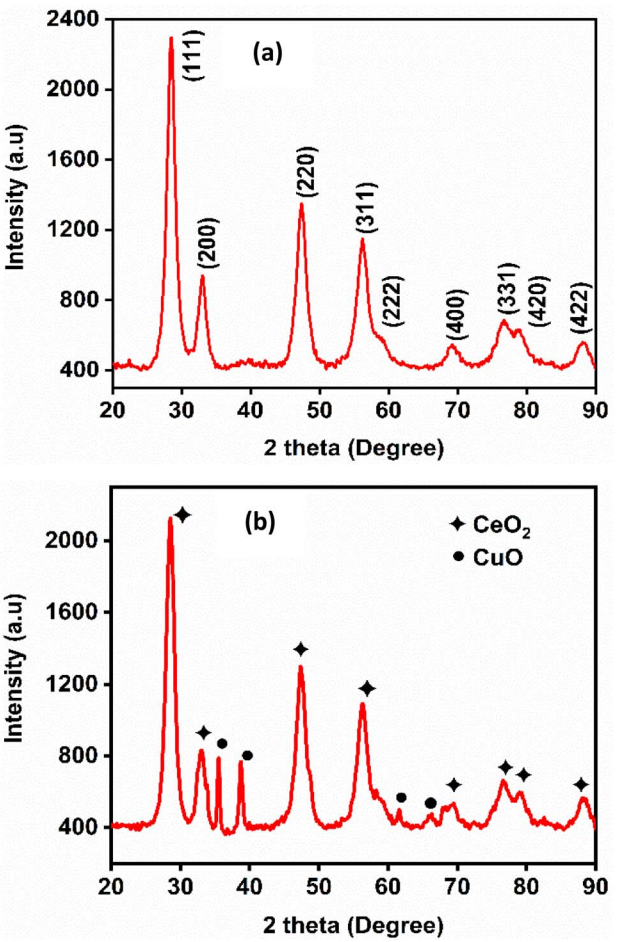

Fig. 3 XRD patterns of (a) nanocrystalline CeO_2 and (b) CeO_2–CuO nanocomposite.

requirement that will enhance the electrochemical performance of the nanomaterials due to its high surface-to-volume ratio and large number of active sites.[40] This intrinsic characteristic of nanomaterials is particularly beneficial in the context of corrosion protection, where a large surface area leads to improved interactions between the protective layer and the corrosive environment. The EDAX spectra of both nano CeO_2 and CeO_2–CuO nanocomposite along with elemental composition are shown in Fig. 2. The characteristic peaks corresponding to cerium, copper and oxygen appearing in the spectra with the expected ratios confirm the successful synthesis of these materials.

3.2.2 Crystallinity and phase structure. The XRD spectrum of CeO_2 displays reasonably sharp diffraction peaks at 2θ values of 28.53°, 32.92°, 47.35°, 56.33°, 58.80°, 69.17°, 76.56°, 78.69° and 88.20° (Fig. 3). These peaks correspond to Miller indices (111), (200), (220), (311), (222), (400), (331), (420) and (422), respectively,[39] indicating a defective face-centred cubic phase of CeO_2 and are consistent with JCPDS no. 34-0394. In the XRD spectrum of the CeO_2–CuO composite (Fig. 3b), the peaks at 35.44°, 38.85°, 61.61° and 66.18° are assigned to the monoclinic phase of CuO corresponding to the (−111), (111), (−113) and (−311) planes, respectively in accordance with JCPDS no. 089-2530. As this XRD pattern includes all characteristic peaks arising from both the defective face-centred cubic phase of CeO_2 and the monoclinic phase of CuO, it confirms the successful formation of CuO within the CeO_2 matrix.[41] The approximate crystallite sizes of nanocrystalline CeO_2 and CeO_2–CuO nanocomposite were found to be 5.2 ± 0.4 nm and 10.6 ± 0.4 nm, respectively, calculated using the Debye–Scherrer eqn (1).

The chemical state and elemental composition of nanocrystalline CeO_2 and CeO_2–CuO nanocomposite were investigated using XPS and the results were illustrated in Fig. 4 and 5, respectively. The survey scan spectrum of CeO_2 identified the presence of C 1s, O 1s, and Ce 3d (Fig. 4a). The XPS spectrum of CeO_2–CuO composite was similar to that of CeO_2: it showed the presence of Cu 3d in addition to all other elements observed for CeO_2 (Fig. 5a). The elemental compositions derived from the XPS survey scans for both CeO_2 and CeO_2–CuO are shown in the respective figures: the data are consistent with the size of the elements and composition of the materials. In the high-resolution Ce 3d spectrum of both CeO_2 and CeO_2–CuO composite (Fig. 4b and 5b, respectively), eight peaks were observed corresponding to the spin–orbit splitting of Ce $3d_{5/2}$ and Ce $3d_{3/2}$. This indicates that CeO_2 contains both Ce^{3+} and

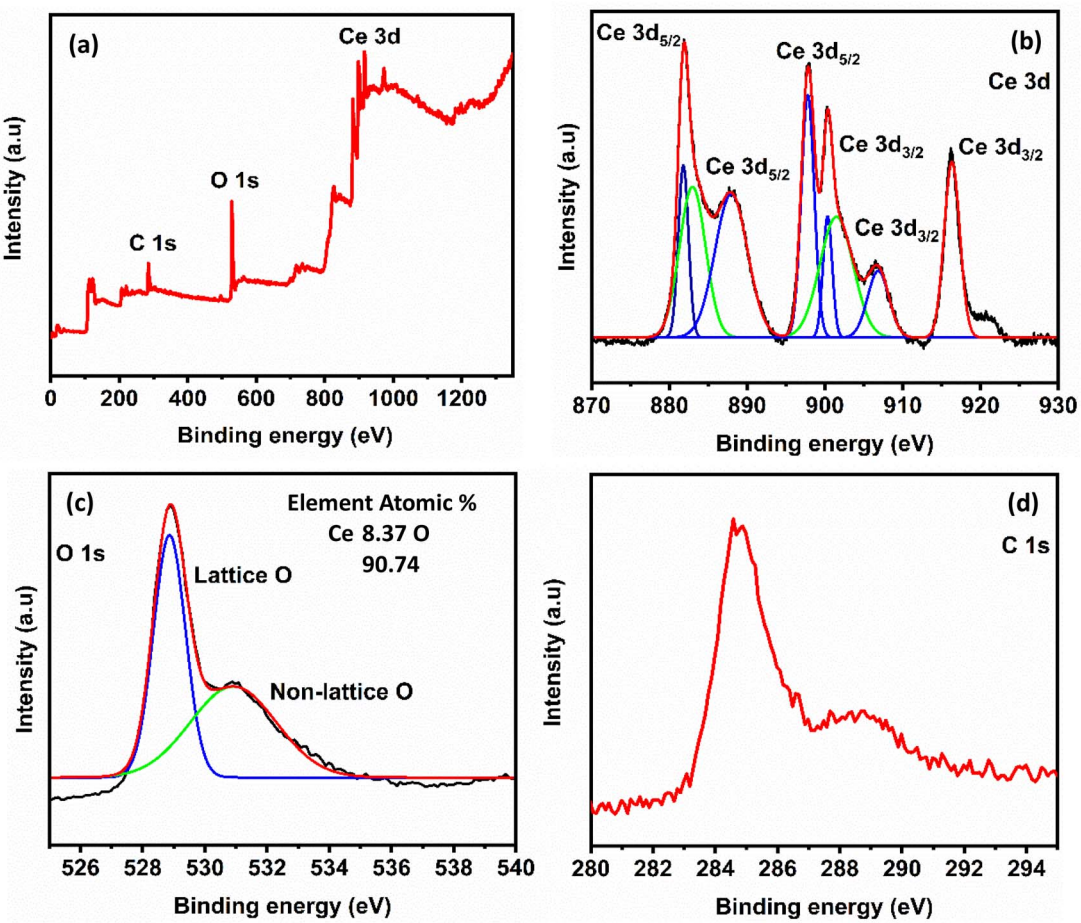

Fig. 4 (a) XPS spectrum of nanocrystalline CeO_2, (b) high resolution spectrum of Ce 3d, (c) high resolution spectrum of O 1s and (d) high resolution spectrum of C 1s.

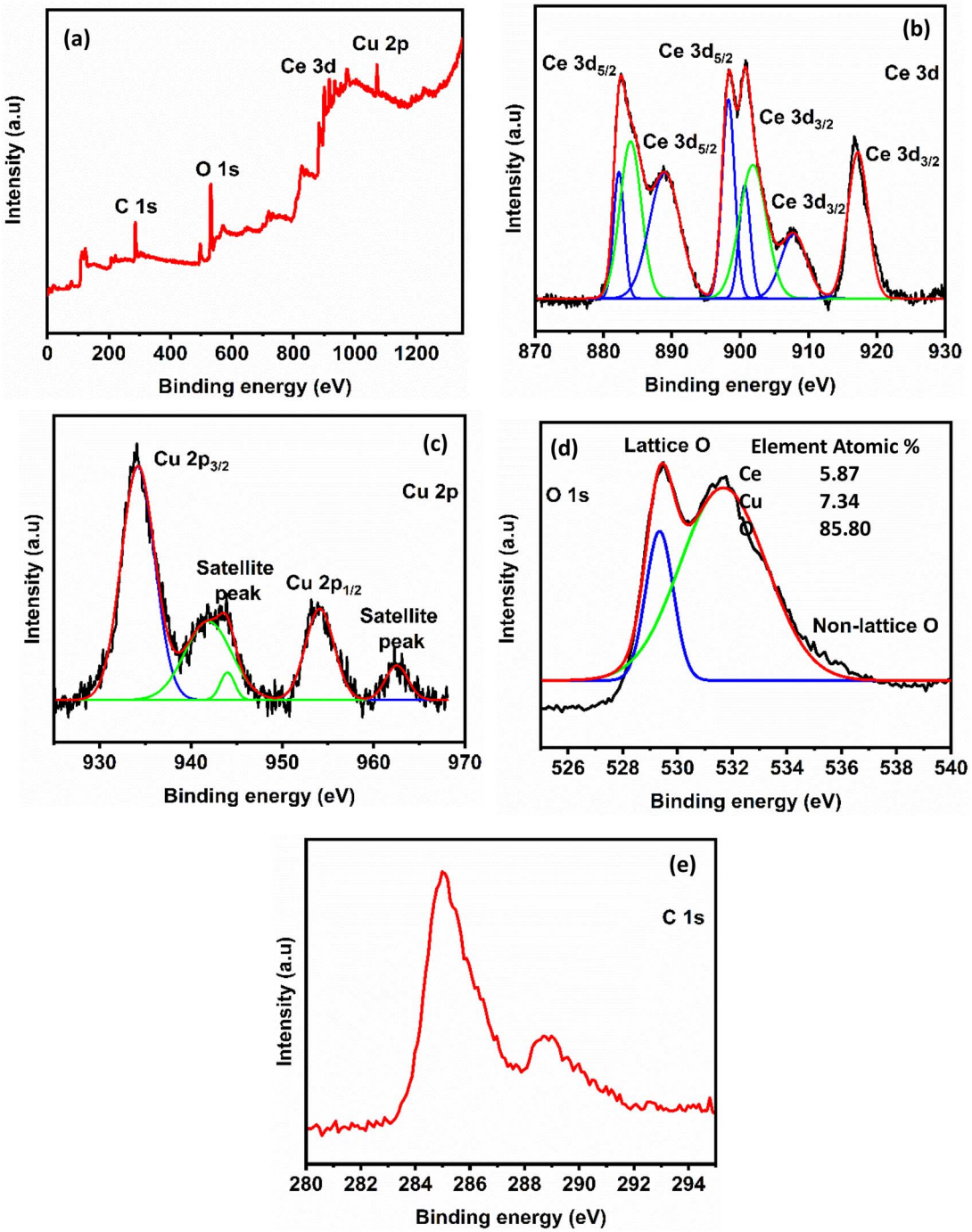

Fig. 5 (a) XPS spectrum of CeO_2–CuO nanocomposite, (b) high resolution spectrum of Ce 3d, (c) high resolution spectrum of Cu 2p, (d) high resolution spectrum of O 1s and (e) high resolution spectrum of C 1s.

Ce^{4+} oxidation states. The six distinct peaks with binding energy values at 881.8, 888.0, 898.0, 900.4, 906.4, and 916.2 eV are associated with the Ce^{4+} 3d state, confirming the predominant valence state of Ce as +4. The two weak XPS peaks at the binding energy values of 883.1 and 901.9 eV correspond to the Ce^{3+} oxidation state.[42,43] The observed yellowish colour of CeO_2 supports the presence of both Ce^{4+} and Ce^{3+} ions in the structure.[44] In the CeO_2–CuO composite, two significant peaks appeared at 933.9 eV and 953.7 eV: these values are the binding energies of Cu $2p_{3/2}$ and Cu $2p_{1/2}$, respectively (Fig. 5c). The three satellite peaks in the XPS spectrum of Cu^{2+} at binding energies of 941.0 eV, 943.6 eV and 962.3 eV indicate a partially filled d-block configuration ($3d^9$) for Cu^{2+} in the ground state.[45,46] The high-resolution XPS spectra of O 1s of both CeO_2 and CeO_2–CuO composite revealed two peaks: the first peak around 528.8 eV originated from lattice oxygen and the peak of higher binding energy (531.1 eV) is attributed to physically adsorbed oxygen and/or a hydroxyl group. In both of the cases,

the C 1s peaks correspond to the carbonate impurities present in the compounds.

3.2.3 Thermal properties. From the TGA curves shown in Fig. S4 (ESI),† it can be seen that both of the compounds undergo single-stage weight loss up to 700 °C. An initial weight loss of 5% in the case of CeO_2 and 8% in the case of CeO_2–CuO composites observed below 100 °C is primarily due to the evaporation of trapped moisture.[35] The indistinguishably observed meagre and gradual weight loss of 4% in CeO_2 and 3% in the CeO_2–CuO composite at temperatures ranging from 100 °C to 500 °C is attributed to the release of carbon dioxide adsorbed from the atmosphere and decomposition of the residual nitrate present in the compounds. FT-IR spectral analyses confirm this observation. The endothermic peak detected below 100 °C in the DTA curves of both of the compounds is indicative of water evaporation. In the absence of any other transitions in the DTA curves, these results together with the TGA results confirm that these compounds are stable up to the studied temperature of 700 °C.

3.3 Characterization of the coatings

3.3.1 Bonding characteristics, crystallinity and phase composition. FT-IR spectra of the unmodified zinc phosphate coating and representative spectrum of coatings modified with nanocrystalline CeO_2 and CeO_2–CuO nanocomposite are given in Fig. S5 (ESI).† They showed characteristic absorption bands for different functional groups present in the coatings. The bands appearing at around 3165 cm^{-1} and 1620 cm^{-1} are respectively attributed to O–H stretching and H–O–H bending vibrations of water molecules. These broad bands are indicative of the hydrated nature of phosphate crystals formed. The bands observed at 1126 cm^{-1} and 1029 cm^{-1} are associated with the asymmetric stretching vibrations of HPO_4^{2-} and PO_4^{3-} groups, respectively. The peak at 922 cm^{-1} arises from ν_1 P–O symmetric stretching of HPO_4^{2-}. Lastly, the absorption at 570 cm^{-1} corresponds to O–P–O bending vibrations. These observations are consistent with previous work and confirm the formation of a protective layer of phosphate on the metal surface.[24,47]

The crystallinity and phase composition of the coatings were studied using XRD and the obtained diffraction patterns are shown in Fig. 6. There are two crystal phases in all the zinc phosphate coatings: the first one is hopeite ($Zn_3(PO_4)_2 \cdot 4H_2O$, JCPDS file 37-0465), which is a major phase and the other one is phosphophyllite ($Zn_2Fe(PO_4)_2 \cdot 4H_2O$, JCPDS file 29-1427), which is a minor phase.[5] After comparing the XRD patterns of unmodified zinc phosphate coating and those modified with nanocrystalline CeO_2 and CeO_2–CuO nanocomposite, it was evident that the addition of both of the additives resulted in stronger (high intensity) reflections for the hopeite phase and this was more significant in the case of coatings formulated with CeO_2–CuO nanocomposite. The strong reflection observed at 19.5° correspond to the (020) plane of hopeite crystals.[22] This increase in intensity indicates that the additives play a vital role in the formation of the phosphate coating layer. The diffraction peak for the phosphophyllite phase appeared at 31.5°, but was weak in the case of coating containing CeO_2 and very weak in

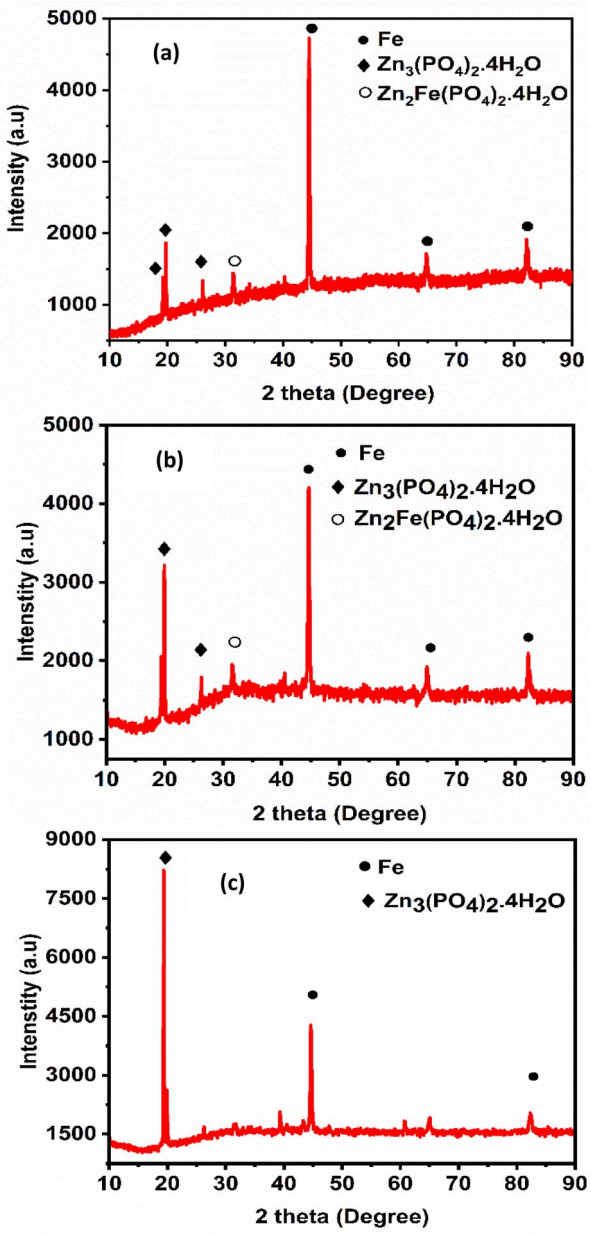

Fig. 6 XRD pattern of zinc phosphate coating corresponding to (a) ZnP, (b) ZnP-0.6CO and (c) ZnP-0.3COCO.

the CeO_2–CuO modified coatings. Further, the XRD patterns reveal a considerable reduction in the intensity of iron upon the addition of nanocrystalline CeO_2 and CeO_2–CuO nanocomposite, suggesting improved surface coverage and enhanced growth of hopeite.[48] The absence of shifts in the 2 theta values of the major components confirms that the addition of these additives did not affect the phase composition of phosphate crystals while influencing its growth. The sizes of the phosphate crystallites were 32.9 ± 0.4 nm, 19.3 ± 0.8 nm and 18.1 ± 0.4 nm for ZnP, ZnP-0.6CO and ZnP-0.3COCO, respectively. These results together with the SEM micrograph showed that both of the nanometal oxides enhanced the nucleation sites, reduced the crystal size and resulted in coatings with more phosphate crystals.

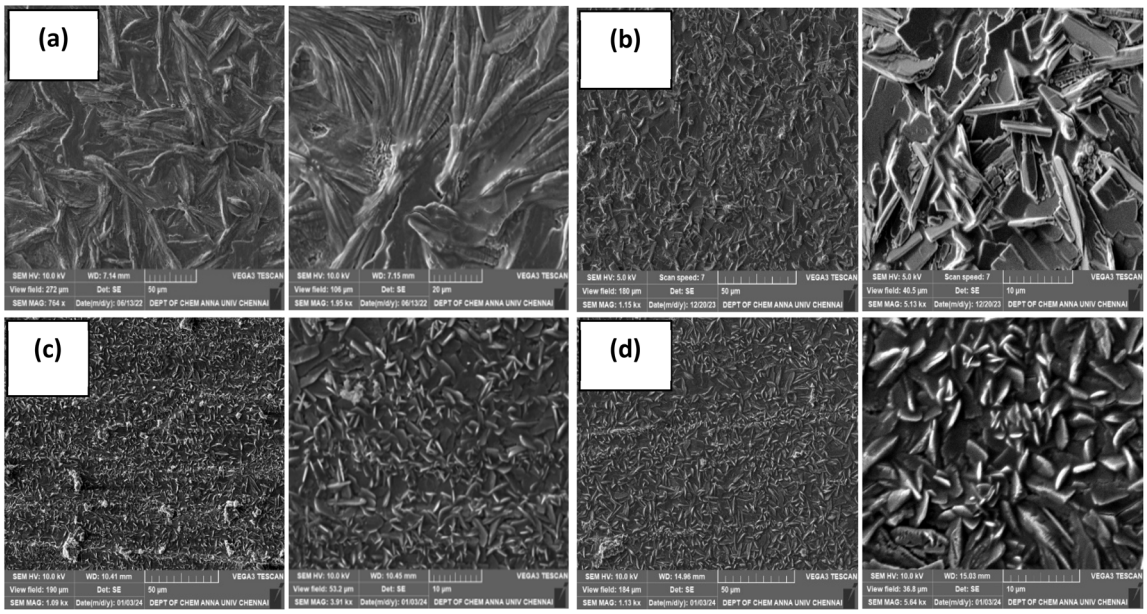

Fig. 7 Surface morphology of zinc phosphate coating formulated with different amounts of nanocrystalline CeO_2. (a) ZnP; (b) ZnP-0.3CO; (c) ZnP-0.6CO; and (d) ZnP-0.9CO (right side images are magnified, scale bar = 10 μm).

3.3.2 Morphology and elemental compositions of the coatings. Fig. 7 and 8 illustrates the surface morphology of the zinc phosphate coatings modified with different amounts (0.3–0.9 g) of nanocrystalline CeO_2 and CeO_2–CuO nanocomposite. FE-SEM images of the coating without these additives reveal that the coating is uneven and the formed hopeite crystals are oriented and large in size. The images also confirmed the presence of numerous cracks in the coatings, which were caused by the stress developed due to hydrogen evolution during the crystallisation process.[22,49] These cracks allow the electrolyte to penetrate the coating and potentially lead to corrosion. In contrast to the unmodified coating, the zinc phosphate coating modified with nanocrystalline CeO_2 and CeO_2–CuO nanocomposites exhibits distinct changes in morphology and crystal structure; the formed crystals are dense, well defined and randomly oriented across the surface. The hopeite crystals formed in the coating formulated with CeO_2 show plate-like structures, whereas some of these crystals formed with the addition of CeO_2–CuO nanocomposites have a cubic-prismatic morphology, indicating unique crystallisation

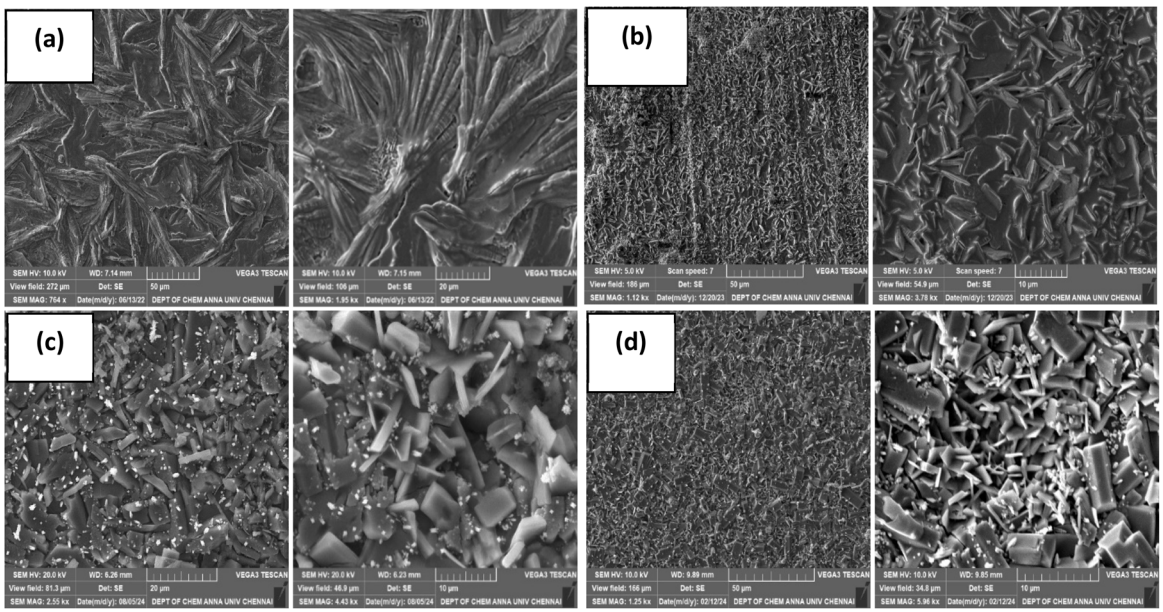

Fig. 8 Surface morphology of zinc phosphate coating formulated with different amounts of CeO_2–CuO nanocomposite. (a) ZnP; (b) ZnP-0.3COCO; (c) ZnP-0.6COCO; and (d) ZnP-0.9COCO (right side images are magnified, scale bar = 10 μm).

Table 2 EDAX-elemental composition of zinc phosphate coating formulated with different amounts of nanocrystalline CeO_2 and CeO_2–CuO nanocomposite

		Elemental composition (in wt%)					
Coating ID	Nanoadditive added	Zn	Fe	P	O	Ce	Cu
ZnP	Nil	21.30	15.40	24.16	38.00	—	—
ZnP-0.3CO	Nano CeO_2	34.16	11.99	18.33	30.31	3.53	—
ZnP-0.6CO	Nano CeO_2	36.29	3.18	20.87	31.63	5.61	—
ZnP-0.9CO	Nano CeO_2	34.85	8.64	19.84	33.04	2.44	—
ZnP-0.3COCO	CeO_2–CuO nanocomposite	39.75	1.39	18.37	24.70	1.85	12.53
ZnP-0.6COCO	CeO_2–CuO nanocomposite	39.06	2.98	19.33	31.97	3.05	3.00
ZnP-0.9COCO	CeO_2–CuO nanocomposite	39.40	1.64	19.69	28.33	4.76	6.21

behaviour. These crystals grow perpendicularly from the steel surface and differ in sizes.[10] Among the three concentration variations in two additives, ZnP-0.6CO and ZnP-0.3COCO produced uniform coatings with relatively smaller crystallites. It can be concluded from the explicit FE-SEM pictures that these nanometal oxide additives act as nucleation sites and produce more compact and dense coating.[50] The SEM micrographs also evidenced that both the additives reduced the cracks that were seen in the unmodified zinc phosphate coating.

The EDAX mapping spectra of all the zinc phosphate coatings are presented in Fig. S6 and S7 (ESI)† and the elemental composition data obtained thereof are given in Table 2. All the spectra confirm the presence of zinc, phosphorus, iron and oxygen present in all the coatings, whereas the spectra of coatings modified with CeO_2 and CeO_2–CuO show the presence of cerium and copper in addition to all those elements. This indicates the successful incorporation of the additives into the zinc phosphate matrix which is essential for enhancing the coating's protective properties.

The zinc and iron content play a crucial role in determining the overall performance of the coating. As shown in Table 2, the zinc content is higher in the modified coatings than in the unmodified coatings, indicating a greater precipitation of zinc phosphate crystals. Another key observation is the low iron content in the modified coating: iron comes from the uncovered metal surface due to the porous nature of the coatings.[25] The low iron content of the modified zinc phosphate coating compared with the unmodified coating suggests that the nanocrystalline CeO_2 and CeO_2–CuO nanocomposite improves the surface coverage and integrity of the coatings.[24] Within the variations in the additives and their concentrations, the increase in zinc content and decrease in iron content is more pronounced in the coatings formulated with 0.6 g L^{-1} of CeO_2 and 0.3 g L^{-1} of CeO_2–CuO nanocomposites.

3.3.3 Coating weight and hardness. The additive effect of synthesized nanocrystalline CeO_2 and CeO_2–CuO composite on these properties of coatings was studied and the results were listed in Table 3. The data clearly indicate an increase in the coating weight against the addition of nanometal oxide additives. Upon adding the minimum quantity (0.3 g L^{-1}) of nano CeO_2 to the phosphating bath, the coating weight increased from 4.8 ± 0.1 g m^{-2} to 13.8 ± 0.2 g m^{-2}, although the coating weight decreased upon further addition of nano CeO_2. On the other hand, in the case of coatings based on CeO_2–CuO nanocomposite, the coating weight successively increased up to 20.1 ± 0.8 g m^{-2} for the 0.6 g L^{-1} additive and then slightly decreased. This increase in coating weight against metal oxide additives can be attributed to an larger number of cathodic sites that facilitates the formation of phosphate crystals.[18,51] This can be further claimed with the formation of additional nucleation sites, which leads to a denser and more compact coating structure.[11]

The micro hardness of all the coatings was determined and the values were included in Table 3. In both of the series of coatings, the hardness increased with greater concentrations of nanoadditives. The highest hardness was achieved for the coating formulated with 0.9 g L^{-1} of CeO_2–CuO (173.8 ± 5.8 HV), which is 20.1 HV higher than that of unmodified coating. This improved hardness of the zinc phosphate coating modified with nano CeO_2 and CeO_2–CuO nanocomposite indicate that

Table 3 Weight and hardness of zinc phosphate coating formulated with different amounts of nanocrystalline CeO_2 and CeO_2–CuO nanocomposite

Coating ID	Nanoadditive added	Coating weight (g m^{-2})	Micro hardness (HV)
ZnP	Nil	4.8 ± 0.1	153.7 ± 2.9
ZnP-0.3CO	Nano CeO_2	13.8 ± 0.2	159.9 ± 1.7
ZnP-0.6CO	Nano CeO_2	12.0 ± 0.4	166.2 ± 5.9
ZnP-0.9CO	Nano CeO_2	10.8 ± 0.2	169.0 ± 3.7
ZnP-0.3COCO	CeO_2–CuO nanocomposite	17.4 ± 0.5	158.0 ± 3.1
ZnP-0.6COCO	CeO_2–CuO nanocomposite	20.1 ± 0.8	166.6 ± 6.4
ZnP-0.9COCO	CeO_2–CuO nanocomposite	19.4 ± 0.4	173.8 ± 5.8

significant changes occurred in the microstructure of hopeite crystals.

3.3.4 Wettability and adhesion. For a coating to combat corrosion effectively, it should repel water or any other corrosive agents. Therefore, it should be hydrophobic or neutral. The water contact angles of the coatings formulated for the present work are shown in Fig. S8 (ESI).† The zinc phosphate coating without metal oxide additives showed a hydrophilic character with a contact angle of 39.9°. The addition of nanocrystalline CeO_2 and CeO_2–CuO nanocomposite significantly improved the contact angle towards a neutral value: a maximum contact angle of 62.9° was obtained for the addition of 0.3 g L^{-1} of CeO_2. Upon increasing the concentration, the contact angle of the coating decreased. The opposite trend was observed in the case of CeO_2–CuO based coatings.

Adhesion of a coating with a metal surface plays a crucial role in the coating's protective performance. In corrosive environments, the penetration of corrosive agents into the metal-coating interface weakens the coating's adhesion. The cross-hatch adhesion test images of coated steel substrates were recorded (Fig. S9 and S10, ESI†) and the coating's adhesion strength was assessed according to the ASTM D3359-17 standard. The coating without the additive and the coatings modified with CeO_2 demonstrated good adhesion with no detachment or damage at the grid edges and no squares were eliminated in these coatings during removal of the adhesive tape. Thus, these coatings were rated 5B. On the other hand, the coatings formulated with CeO_2–CuO composite showed trace removal of the coating within the square grids. However, the edges remained intact and it was rated 4B, indicating less than 5% removal. These adhesion test results suggest that the added nanocrystalline CeO_2 and CeO_2–CuO nanocomposite did not interfere with the interactions and bonding force acting between the coating and the steel substrate.

3.3.5 Potentiodynamic polarisation studies. The corrosion resistance of zinc phosphate coatings modified with nanocrystalline CeO_2 and CeO_2–CuO nanocomposite studied by analysing the respective potentiodynamic polarisation curves was depicted in Fig. 9. The corrosion parameters such as corrosion current density (I_{corr}), corrosion potential (E_{corr}), polarisation resistance (R_p), cathodic (β_c) and anodic (β_a) Tafel slopes and the corrosion rate (CR) calculated using the Tafel extrapolation method were given in Table 4. It is evident from the data that the I_{corr} values of all the modified zinc phosphate

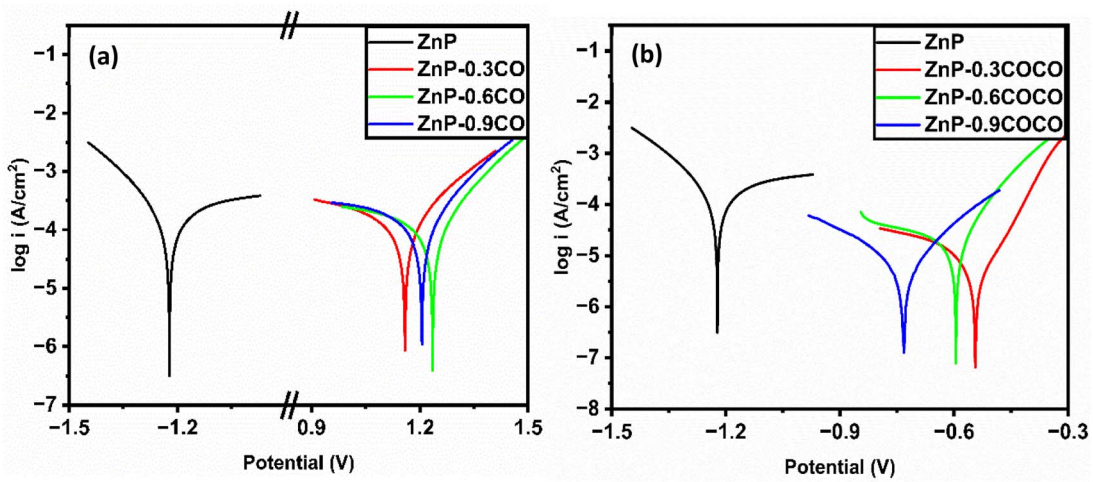

Fig. 9 Potentiodynamic polarisation curves of the uncoated and zinc phosphate coated steel substrates immersed in 3.5% NaCl. Coatings were formulated with different amounts of (a) nanocrystalline CeO_2 and (b) CeO_2–CuO nanocomposite.

Table 4 Electrochemical parameters obtained by Tafel extrapolation of polarisation curves of zinc phosphate coatings formulated with different amounts of nanocrystalline CeO_2 and CeO_2–CuO nanocomposite. Coated mild steel panels were immersed in 3.5% NaCl solution

		Electrochemical parameters					
Coating ID	Nano additive added	I_{corr} (μA cm^{-2})	E_{corr} (V)	β_a (V dec^{-1})	$-\beta_c$ (V dec^{-1})	R_p (ohm cm^2)	Corrosion rate (CR) (mm per year)
ZnP	Nil	156.2	1.22	0.500	0.167	348	1.843
ZnP-0.3CO	Nano CeO_2	87.44	1.16	0.155	0.333	525	1.032
ZnP-0.6CO	Nano CeO_2	44.80	1.24	0.191	0.271	1086	0.528
ZnP-0.9CO	Nano CeO_2	65.10	1.21	0.167	0.258	676	0.768
ZnP-0.3COCO	CeO_2–CuO nanocomposite	3.025	−0.54	0.087	0.111	7003	0.036
ZnP-0.6COCO	CeO_2–CuO nanocomposite	17.50	−0.59	0.106	0.500	2169	0.207
ZnP-0.9COCO	CeO_2–CuO nanocomposite	3.98	−0.73	0.099	0.139	6321	0.047

coatings are low compared with that of unmodified coating. Furthermore, the proportional decrease in the corrosion rate in the modified coatings suggests better corrosion protection. The slightly high E_{corr} value of coating modified with 0.6 g L^{-1} of CeO_2 compared with the unmodified coating indicates better corrosion resistance of this coating. Although the E_{corr} values of all the CeO_2–CuO composite modified coatings shifted to a negative direction, these parameters are best evaluated through R_p and CR. The R_p and CR of the coating without the additive are 348 Ω cm^2 and 1.843 mm per year, respectively. Upon the addition of nanocrystalline CeO_2 and CeO_2–CuO nanocomposite to the coating recipe, both of these parameters improved significantly. In the case of coatings with CeO_2, higher R_p (1086 Ω cm^2) and lower CR (0.528 mm per year) were observed at the additive concentration of 0.6 g L^{-1}. In comparison, coatings with the CeO_2–CuO composite showed more significant improvement even at a low additive concentration of 0.3 g L^{-1}. These results reveal that both nanocrystalline CeO_2 and CeO_2–CuO nanocomposite increase the ability of the zinc phosphate coating to retard the electrochemical reaction occurring at the electrode–electrolyte interface and thereby increase the corrosion resistance, especially the CeO_2–CuO nanocomposite. This improved corrosion resistance of all the modified coatings perceived from the polarisation studies is mainly due to formation of dense and compact coatings.

3.3.6 Electrochemical impedance spectroscopy (EIS). To further assess the protective properties of modified zinc phosphate coatings, EIS was employed and the Nyquist plots, Bode phase angles and Bode magnitude plots of the coatings formulated with nanocrystalline CeO_2 and CeO_2–CuO nanocomposite are displayed in Fig. 10 and 11, respectively. The high frequency region of the Nyquist plot revealed the barrier properties of the coating, while the low-frequency regions corresponded to the diffusion-controlled corrosion reaction taking place at the coating and steel surface interface.[52] The Nyquist plot of the coating without metal oxide additive shows two capacitive loops, whereas that of each CeO_2 modified coating has one additional inductive loop. The first is the large capacitive loop at high frequency, followed by a mid-frequency inductive loop and finally a small low frequency capacitive loop.[53] The shape of the Nyquist plots remains the same for all three concentrations of CeO_2. The high frequency capacitive loop is attributed to the zinc phosphate coating and the inductive loop is related with the relaxation of adsorbed species like Cl^- and O^{2-} on the surface of the coating. The capacitive loop at the low frequency region is due to the charge transfer reaction.[31,54] In the case of CeO_2–CuO modified coatings, they

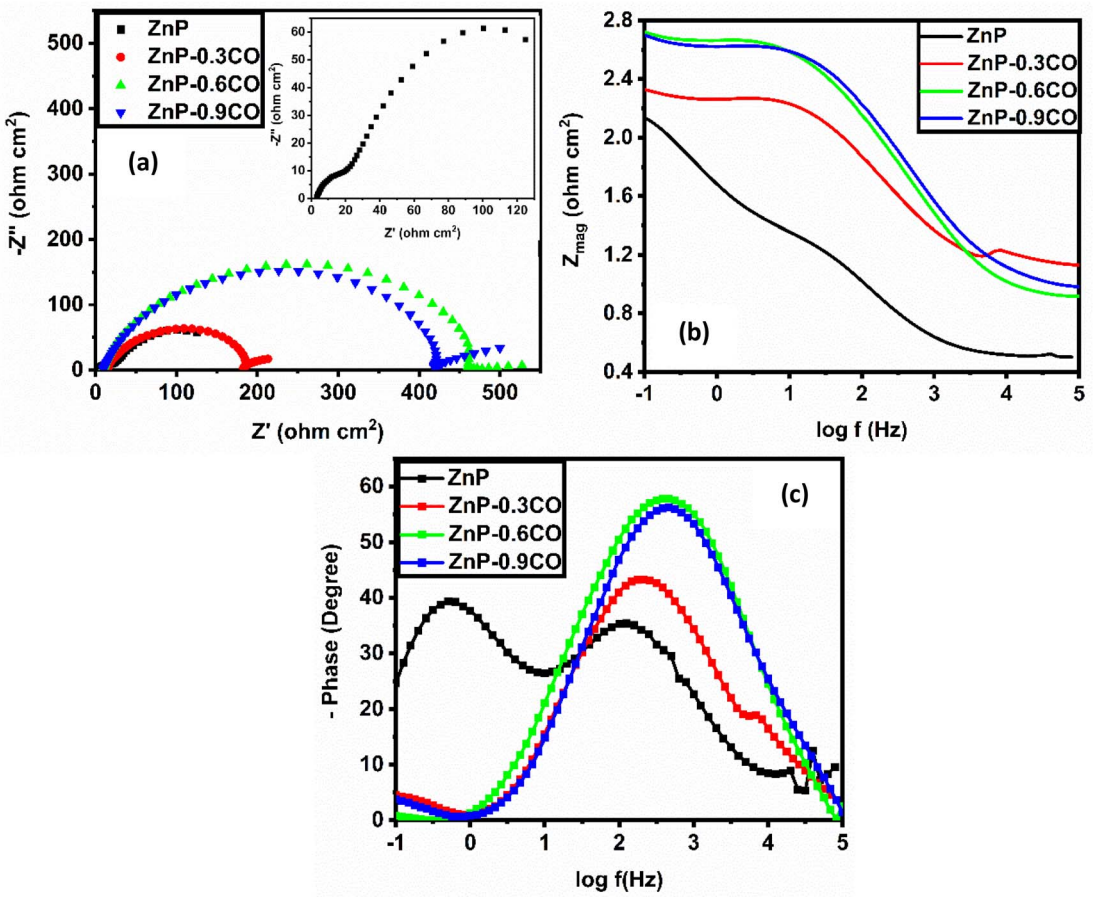

Fig. 10 (a) Nyquist plots, (b) Bode plots and (c) frequency dependence of phase angles *vs.* electrochemical impedance curves of the uncoated and zinc phosphate coated steel substrates immersed in 3.5% NaCl. Coatings were formulated with different amounts of nanocrystalline CeO_2.

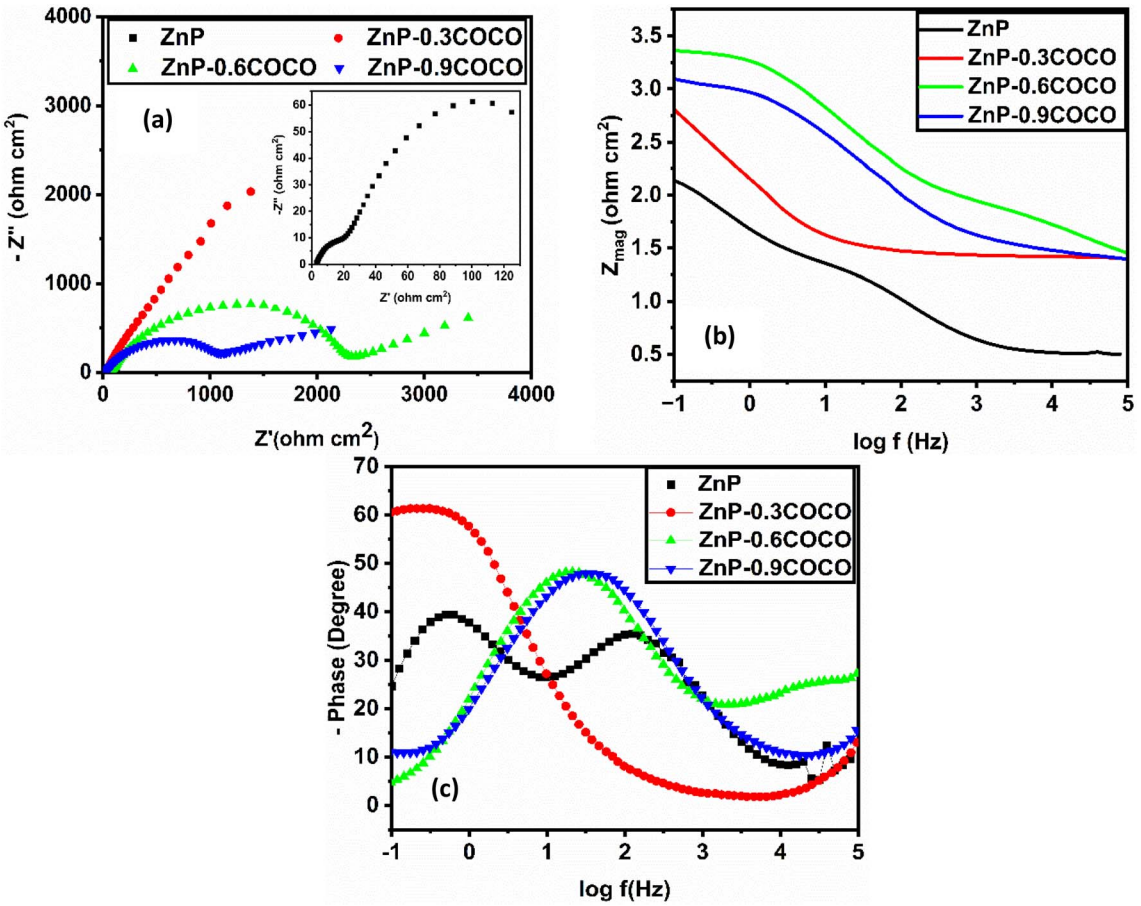

Fig. 11 (a) Nyquist plots, (b) Bode plots and (c) frequency dependence of phase angles *vs.* electrochemical impedance curves of the uncoated and zinc phosphate coated steel substrates immersed in 3.5% NaCl. Coatings were formulated with different amounts of CeO_2–CuO nanocomposite.

have a high frequency capacitive loop followed by low frequency Warburg impedance associated with the diffusion process.

In general, the large diameter of the capacitive loop indicates enhanced corrosion resistance as they reflect greater impedance to ion penetration.[55] For nanocrystalline CeO_2 modified coatings, the diameter of the first capacitive loop increases successively from that without additive to the inclusion of 0.3 g L^{-1} and 0.6 g L^{-1} additive and then decreased. The Bode impedance at the low frequency region corresponds to the barrier properties of the coatings. The higher the impedance modulus, the greater the blocking of corrosive ions by the coating.[22] From Fig. 10b and 11b, it is clear that the impedance modulus increased upon the addition of both CeO_2 and CeO_2–CuO into the coatings. Similarly, these additives increased the phase angle of the coating up to 60°. This indicates that the stability of the modified coatings improved in this impedance measurement condition compared with the unmodified coating.

The impedance curves were fitted to equivalent electrical circuits using ZSimpWin software for further analysis and the generated circuits for unmodified and modified zinc phosphate coatings were given in Fig. 12. From the equivalent circuits, electrochemical parameters including R_s (solution resistance), R_c (coating resistance), R_{ct} (charge transfer resistance), C_c and Q_c (coating capacitance), C_{dl} and Q_{dl} (double layer capacitance)

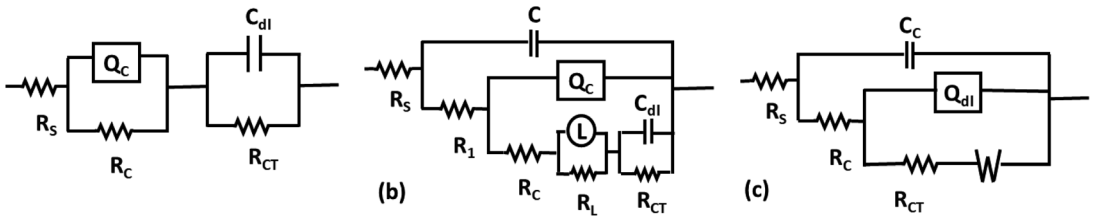

Fig. 12 Equivalent electrical circuit used to obtain the electrochemical parameters from the Nyquist plots of coatings in 3.5% NaCl. (a) ZnP; (b) ZnP-CO (common for three variations) and (c) ZnP-COCO (common for three variations). Fitted curves are given in Fig. S11, ESI.†

and W (Warburg impedance) were obtained and listed in Table 5. In the circuit, L and R_1 are inductive elements. The R_s of all the modified coatings and R_c of all the coatings except the one prepared with 0.9 g L^{-1} of CeO_2–CuO nanocomposite are improved by the addition of metal oxide additives into the coating composition. The low Q_c value of coating containing nanocrystalline CeO_2 indicates a restriction of the penetration of ions, water molecules and oxygen through the coating. This also means that this additive blocks the pores and reduces the porosity of the coating. Importantly, the R_{ct} component of all the modified coatings are higher than that of the unmodified coating, which indicates that the added nanocrystalline CeO_2 and CeO_2–CuO nanocomposite successfully protects the substrate. In the case of CeO_2 modified coatings, a high R_{ct} (427.5 Ω cm^2) was obtained for coating formulated with 0.6 g L^{-1} of this additive and a remarkable enhancement in this parameter was found in the case of coating added with 0.3 g L^{-1} of CeO_2–CuO nanocomposite for which the R_{ct} value (3645 Ω cm^2) was more than thirty-one times higher than the unmodified coating. This parameter represents the resistance towards charge transfer reactions occurring on the electrode. The high R_{ct} indicates that the defects in the coating are reduced due to refinement of hopeite crystals.[25,56] The presence of Warburg elements in the CeO_2–CuO nanocomposite added coatings shows that the corrosion reaction is diffusion controlled. From these EIS studies, it can be concluded that 0.3 g L^{-1} addition of CeO_2–CuO nanocomposite forms more corrosion resistant coating.

3.3.7 Salt spray test. A salt spray test is an accelerated test method used to assess the corrosion resistance of a coating in a simulated experimental condition. All the coatings modified with metal oxide additives were subjected to this standard test and the obtained results were compared with that of the unmodified coating. The recorded photographs after the completion of the tests are displayed in Fig. 13 and the corrosion rate determined from the weight loss data are given in Table 6 along with additive's inhibition efficiency. The observed corrosion products (rust) that formed across the coated surface in the images indicate that the zinc phosphate coating prepared without metal oxide additive has poor corrosion resistance. The introduction of nanocrystalline CeO_2 into the coating significantly reduced the degree of corrosion throughout the coating surface and lowered the corrosion rate at all concentrations used. Analysis of the additives concentration effect showed that ZnP-0.6CO had the lowest CR with the highest inhibition efficiency. This finding aligns with a previous study that describes the potential of using amorphous CeO_2 of particle size ≈ 60 nm as a corrosion inhibitor.[57] When introducing CeO_2–CuO nanocomposite into the coating, a different effect was observed in the corrosion behaviour. At the minimum concentration (0.3 g L^{-1}), the coating was less corroded compared with the coating without the additive and this observation was consistent with the electrochemical characterisation results. Besides, this was supported by a previous study in which copper enhanced the corrosion protection of zinc phosphate coating on an aluminium surface.[58] The corrosion increased with greater concentrations of CeO_2–CuO nanocomposite. This observation contradicted with the potentiodynamic polarisation and electrochemical impedance results. The high corrosion observed in ZnP-0.6COCO and ZnP-0.9COCO indicates that structural changes occurred in these coatings after exposing them to a 5% NaCl solution for a longer time (compared with electrochemical characterisation) during the experiment. As previously discussed, the structural defects at the micro level allows the electrolyte to diffuse into the metal surface and initiates the corrosion. The reason for such structural defects may be due to

Table 5 Fitting values of equivalent electrical circuits of zinc phosphate coatings formulated with different amounts of nanocrystalline CeO_2 and CeO_2–CuO nanocomposite. Coated mild steel panels were immersed in 3.5% NaCl solution

		Fitting values of equivalent electrical circuit						
					Q_c			
Coating ID	Nano additive added	R_s (Ω cm^2)	R_c (Ω cm^2)	R_{ct} (Ω cm^2)	$Y \times 10^{-5}$ (Ω^{-1} S^n cm^{-2})	n	$C_{dl} \times 10^{-2}$ F cm^{-2}	$\chi^2 \times 10^{-3}$
ZnP	Nil	2.98	30.82	114.3	178.9	0.63	0.629	3.44
ZnP-0.3CO	Nano CeO_2	12.69	29.08	167.4	9.928	0.74	3.107	3.21
ZnP-0.6CO	Nano CeO_2	8.34	35.25	427.5	5.498	0.68	0.025	0.92
ZnP-0.9CO	Nano CeO_2	9.62	58.47	400.2	3.510	0.73	1.337	0.75

		Fitting values of equivalent electrical circuit							
						Q_{dl}			
Coating ID	Nano additive added	R_s (Ω cm^2)	R_c (Ω cm^2)	R_{ct} (Ω cm^2)	$C_c \times 10^{-5}$ F cm^{-2}	$Y \times 10^{-5}$ (Ω^{-1} S^n cm^{-2})	n	$W \times 10^{-3}$ (Ω cm^2)	$\chi^2 \times 10^{-3}$
ZnP-0.3COCO	CeO_2–CuO nanocomposite	15.95	11.17	3645	0.10	204.8	0.73	0.53	1.40
ZnP-0.6COCO	CeO_2–CuO nanocomposite	25.27	43.31	2424	0.23	7.38	0.69	6.44	6.19
ZnP-0.9COCO	CeO_2–CuO nanocomposite	19.35	10.73	1179	0.22	12.75	0.69	4.47	3.67

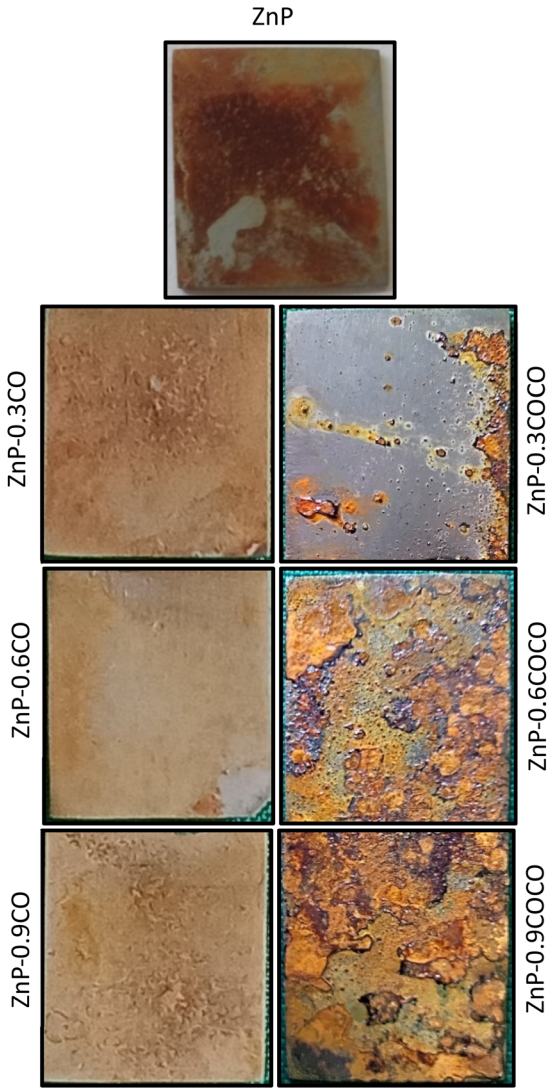

Fig. 13 Salt spray test images of coatings formulated without nano additive (top), with nanocrystalline CeO_2 (left) and with CeO_2–CuO nanocomposite (right).

the formation of an association complex between more cathodic copper (compared with cerium) and chloride ions at high concentration, with subsequent dissolution of copper complex into the salt solution. To verify this, ZnP-0.6COCO was subjected to a salt-spray test for 20 min and 20 h along with its counterpart ZnP-0.6CO and their surfaces were analysed using FE-SEM (Fig. 14). It can be clearly seen that the coating layer of ZnP-0.6CO shows less cracks, whereas that of ZnP-0.6COCO was not affected for 20 min and supports the obtained electrochemical characterisation results. However, the phosphate crystals are solvated in ZnP-0.6COCO exposed to 5% NaCl solution for 20 h, leaving more cracks in the coating surface and confirming the postulated reason.

3.3.8 Mechanism of enhanced corrosion resistance of zinc phosphate coatings in the presence of nanocrystalline CeO_2 and CeO_2–CuO nanocomposite. The size of the formed phosphate crystallites decreased from 32.9 ± 0.4 nm in the unmodified coating to 19.3 ± 0.8 nm and 18.1 ± 0.4 nm when adding nanocrystalline CeO_2 and CeO_2–CuO nanocomposite at concentrations of 0.6 g L^{-1} and 0.3 g L^{-1}, respectively to the phosphate coating bath. At the same time, the intense reflections of crystalline CeO_2 and CuO appearing at $2\theta = 29.1$ and $2\theta = 35.49$, respectively (Fig. 3) were not observed in the XRD patterns of the coatings. This confirms the dissolution of both nano CeO_2 and CeO_2–CuO nanocomposite into the excess phosphoric acid, forming their respective phosphates as shown below:

$$3CeO_2 + 4H_3PO_4 \rightarrow Ce_3(PO_4)_4 + 6H_2O \quad (6)$$

$$3CuO + 2H_3PO_4 \rightarrow Cu_3(PO_4)_2 + 3H_2O \quad (7)$$

The characteristic reflections of these phosphates were not seen in the XRD patterns of the coat. The reason may be (i) the metal oxide additives used were in very low quantity (≈150–600 ppm) and (ii) these phosphates may be in the amorphous phase. Therefore, the cerium and copper phosphates that formed from their oxides have played the role of agents that nucleate the crystallisation and interfere with the crystallization of zinc phosphate into lengthy crystallites by suppressing the diffusion of nutrients for the growth of crystals. This can be supported with FE-SEM results of the coatings in which the formation of zinc phosphate as tiny crystals were evidently seen in large quantities compared with the coating without additive. Obviously, the formation of a dense, compact and uniform crystal layer enhanced the corrosion resistance of the coatings.

Table 6 Corrosion rate and corrosion inhibition efficiency of the zinc phosphate coating formulated with different amounts of nanocrystalline CeO_2 and CeO_2–CuO nanocomposite (data obtained from the salt spray test)

Coating ID	Nanoadditive added	Coating weight loss after 48 h ($\times 10^{-3}$ g cm^{-2})	Corrosion rate (CR) ($\times 10^{-3}$ mpy)	Inhibition efficiency (%)
ZnP	Nil	1.32	1.86	No additive
ZnP-0.3CO	Nano CeO_2	1.20	1.70	8.6
ZnP-0.6CO	Nano CeO_2	0.81	1.14	38.7
ZnP-0.9CO	Nano CeO_2	1.02	1.44	22.5
ZnP-0.3COCO	CeO_2–CuO nanocomposite	1.19	1.68	9.6
ZnP-0.6COCO	CeO_2–CuO nanocomposite	2.36	3.33	Not calculated[a]
ZnP-0.9COCO	CeO_2–CuO nanocomposite	2.58	3.67	

[a] Not calculated, since the corrosion rate of the inhibited systems were higher than that of uninhibited systems.

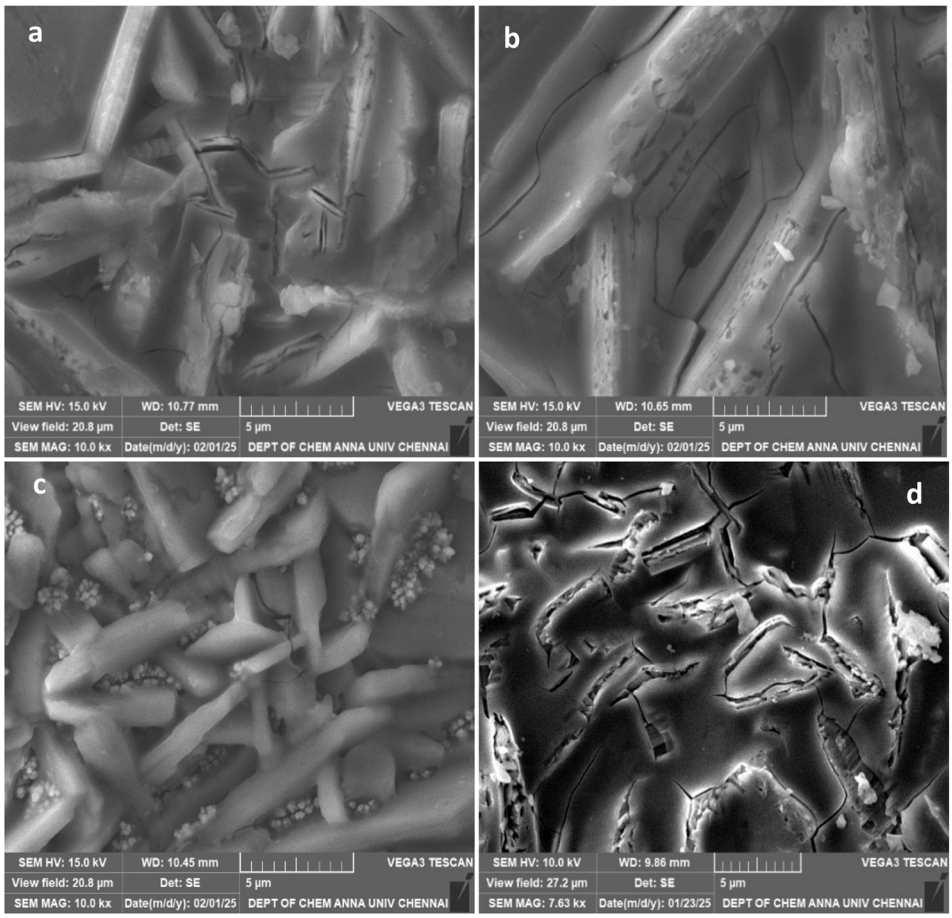

Fig. 14 FE-SEM micrographs of coatings exposed to the salt-spray test. (a and b) Are ZnP-0.6CO exposed to the salt spray test for 20 min and 20 h; (c and d) are ZnP-0.6COCO exposed to the salt spray test for 20 min and 20 h (scale bar for all images = 5 μm).

4. Conclusions

In this systematic study, nanocrystalline CeO_2 and CeO_2–CuO nanocomposite were synthesized and their function as additives to enhance corrosion resistance of zinc phosphate coatings on mild steel substrates in 3.5% NaCl solution was evaluated. The XRD patterns of the coatings revealed that the addition of these compounds decreased the iron content (improved the surface coverage) and enhanced the growth of phosphate crystals without affecting the hopeite–phosphophyllite phase composition in the coatings. The XRD pattern and FE-SEM results revealed that these nanometal oxide additives act as nucleation sites and produced compact coating with more phosphate crystals. The SEM micrographs also revealed that both of these additives reduced the cracks that were seen in the coating prepared without the additive. Among the two metal oxides used in three different concentrations, 0.6 g L^{-1} and 0.3 g L^{-1} was found to be optimum for nanocrystalline CeO_2 and CeO_2–CuO nanocomposite, respectively. It was found that (i) the iron content in the coating decreased from 15.4 wt% (ZnP) to 3.18 wt% upon the addition of CeO_2 and this value was lower following the addition of CeO_2–CuO (1.39 wt%); (ii) the zinc content of the coating increased from 21.3 wt% (ZnP) to 36.29 wt% and 39.75 wt%, respectively following the addition of CeO_2 and CeO_2–CuO; and (iii) the corrosion rate decreased from 1.843 mm per year (ZnP) to 0.528 mm per year and 0.036 mm per year following the addition of nanocrystalline CeO_2 and CeO_2–CuO nanocomposite, respectively. Based on the cross-hatch adhesion test, the coating without the additive and the coatings modified with CeO_2 were rated as 5B and the coatings formulated with CeO_2–CuO composite were rated as 4B. From the results of all the coating characterizations including the accelerated salt-spray test, it was concluded that both of the nanocompounds act as potential corrosion inhibitors, except for the results of the salt-spray test carried out for coatings formulated with higher amounts of CeO_2–CuO nanocomposite, and all the results confirmed that the CeO_2–CuO nanocomposite showed more potential than nanocrystalline CeO_2.

Data availability

All the data related to this research work have been included in this article and in the ESI section.†

Author contributions

S. Ayesha Barsana: conceptualization, methodology, investigation, visualization, analysis and writing – original draft. M. J.

Umapathy: supervision, resources, investigation, methodology, data curation, reviewing and editing. A. Sultan Nasar: methodology, data curation and writing – original draft.

Conflicts of interest

The authors declare no conflicts of interest.

Acknowledgements

The authors acknowledge the characterisation facilities provided by the Sophisticated Instrumentation Facility, Department of Chemistry, College of Engineering, Guindy, Anna University, India.

References

1 D. D. Thiruvoth and M. Ananthkumar, Evaluation of cerium oxide nanoparticle coating as corrosion inhibitor for mild steel, *Mater. Today: Proc.*, 2021, **49**, 2007–2012.
2 A. Kawsihan, D. M. S. N. Dissanayake, N. P. W. Rathuwadu, H. C. S. Perera, K. E. D. Y. T. Dayananda, K. R. Koswattage, R. Mahadeva, A. Ganguly, G. Das and M. M. M. G. P. G. Mantilaka, Synthesis of an eco-inspired anticorrosive composite for mild steel applications, *RSC Adv.*, 2023, **13**, 28852–28860.
3 A. Shukla, B. Sivakumar and S. K. Mishra, Corrosion behavior of Ti-Si-B-C nanocomposite hard coating with different Si contents on 4130 steel, *Metall. Mater. Trans. A*, 2020, **51**, 3576–3586.
4 M. Tamilselvi, P. Kamaraj, M. Arthanareeswari and S. Devikala, Nano zinc phosphate coatings for enhanced corrosion resistance of mild steel, *Appl. Surf. Sci.*, 2015, **327**, 218–225.
5 Y. Xie, M. Chen, D. Xie, L. Zhong and X. Zhang, A fast, low temperature zinc phosphate coating on steel accelerated by graphene oxide, *Corros. Sci.*, 2017, **128**, 1–8.
6 L. Zhang, X. Tong, J. Lin, Y. Li and C. Wen, Enhanced corrosion resistance *via* phosphate conversion coating on pure Zn for medical applications, *Corros. Sci.*, 2020, **169**, 2–8.
7 J. Liu, B. Zhang, W. H. Qi, Y. G. Deng and R. D. K. Misra, Corrosion response of zinc phosphate conversion coating on steel fibers for concrete applications, *J. Mater. Res. Technol.*, 2020, **9**, 5912–5921.
8 C. V. Geethanjali, L. Elias, B. I. Bijimol and S. M. A. Shibli, Strategic enhancement of antimicrobial activity of zinc phosphate conversion coatings through effective integration of P-doped MoS_2 nanoparticles for marine applications, *J. Environ. Chem. Eng.*, 2024, **12**, 114155.
9 C. Jiang, X. Zhang, D. Wang, L. Zhang and X. Cheng, Phosphate conversion coatings on 35CrMnSi steels subjected to different heat treatments, *Electrochem. Commun.*, 2020, **110**, 106636.
10 C. Jiang, G. Xiao, X. Zhang and R. Zhu, Formation and corrosion resistance of a phosphate chemical conversion coating on medium carbon low alloy steel, *New J. Chem.*, 2016, 1347–1353.
11 K. Abdalla, H. Zuhailawati, A. Rahmat and A. Azizan, Characteristics of zinc phosphate coating activated by different concentrations of nickel acetate solution, *Metall. Mater. Trans. A*, 2017, **48**, 771–779.
12 H. Y. Su and C. S. Lin, Effect of additives on the properties of phosphate conversion coating on electrogalvanized steel sheet, *Corros. Sci.*, 2014, **83**, 137–146.
13 N. Van Phuong, K. H. Lee, D. Chang and S. Moon, Effects of Zn^{2+} concentration and pH on the zinc phosphate conversion coatings on AZ31 magnesium alloy, *Corros. Sci.*, 2013, **74**, 314–322.
14 B. Herbáth, K. Kovács, M. Jakab and É. Makó, Crystal structure and properties of zinc phosphate layers on aluminum and steel alloy surfaces, *Crystals*, 2023, **13**, 1–15.
15 M. Golabadi, M. Aliofkhazraei, M. Toorani and A. S. Rouhaghdam, Corrosion and cathodic disbondment resistance of epoxy coating on zinc phosphate conversion coating containing Ni^{2+} and Co^{2+}, *J. Ind. Eng. Chem.*, 2017, **47**, 154–168.
16 J. S. Daubert, G. T. Hill, H. N. Gotsch, A. P. Gremaud, J. S. Ovental, P. S. Williams, C. J. Oldham and G. N. Parsons, Corrosion protection of copper using Al_2O_3, TiO_2, ZnO, HfO_2, and ZrO_2 atomic layer deposition, *ACS Appl. Mater. Interfaces*, 2017, **9**, 4192–4201.
17 V. Dias, H. Maciel, M. Fraga, A. O. Lobo, R. Pessoa and F. R. Marciano, Atomic layer deposited TiO_2 and Al_2O_3 thin films as coatings for aluminum food packaging application, *Materials*, 2019, **12**, 682.
18 M. Tamilselvi, P. Kamaraj, M. Arthanareeswari, S. Devikala and J. A. Selvi, Development of nano SiO_2 incorporated nano zinc phosphate coatings on mild steel, *Appl. Surf. Sci.*, 2015, **332**, 12–21.
19 M. Tamilselvi, P. Kamaraj, M. Arthanareeswari, S. Devikala and J. Arockiaselvi, Effect of nano ZrO_2 on nano zinc phosphating of mild steel, *Mater. Today: Proc.*, 2018, **5**, 8880–8888.
20 N. S. Bagal, V. S. Kathavate and P. P. Deshpande, Nano-TiO_2 phosphate conversion coatings – A chemical approach, *Electrochem. Energy Technol.*, 2018, **4**, 47–54.
21 M. Eskandari, A. Shanaghi, M. Kamani and M. A. Niari, Effect of nano-metal oxides (ZnO, Al_2O_3, CuO, and TiO_2) on the corrosion behavior of a nano-metal oxide/epoxy coating applied on the copper substrate in the acidic environment, *Appl. Nanosci.*, 2021, **11**, 1605–1615.
22 A. H. Riyas, C. V. Geethanjali, S. Arathy, A. Anil and S. M. A. Shibli, Exploration and tuning of Al_2O_3/Mo composite for enhancement of anti-corrosion and tribological characteristics in zinc phosphate conversion coatings, *Appl. Surf. Sci.*, 2022, **593**, 153370.
23 V. A. Bautin, I. V. Bardin, A. R. Kvaratskheliya, S. V. Yashchuk and E. V. Hristoforou, Effect of graphene oxide addition on the anticorrosion properties of the phosphate coatings in neutral and acidic aqueous media, *Materials*, 2022, **15**, 6588.
24 E. Soroush, A. Davarpanah, M. Keramatinia, N. Nouri and B. Ramezanzadeh, Synergistic impact of the functionalized graphene oxide (fGO) nano-sheets and Mn^{2+}-doped zinc phosphate conversion film on the polyester coating

corrosion protection properties, *Colloids Surf., A*, 2023, **678**, 132510.
25 H. Huang, H. Wang, Y. Xie, D. Dong, X. Jiang and X. Zhang, Incorporation of boron nitride nanosheets in zinc phosphate coatings on mild steel to enhance corrosion resistance, *Surf. Coat. Technol.*, 2019, **374**, 935–943.
26 P. Jain, B. Patidar and J. Bhawsar, Potential of nanoparticles as a corrosion inhibitor: A review, *J. Bio Tribo-Corros.*, 2020, **6**, 43.
27 Y. Zhou, J. Xiong and F. Yan, The preparation and characterization of a nano-CeO_2/phosphate composite coating on magnesium alloy AZ91D, *Surf. Coat. Technol.*, 2017, **328**, 335–343.
28 M. J. Deepa, S. R. Arunima and S. M. A. Shibli, Hydrophobic and corrosion-resistant composite ($BiVO_4$/TiO_2) hot-dip zinc coating with enhanced self-cleaning ability, *J. Alloys Compd.*, 2022, **924**, 166522.
29 J. Antonio, C. Mendez, Y. Meas, J. De Jesús and P. Bueno, Cerium and other rare earth salts as corrosion inhibitors – A review, *Prot. Met. Phys. Chem. Surf.*, 2022, **58**, 801–810.
30 S. Zhang, L. Liu, Q. Lei, T. Zhang, J. Bing and J. Dong, A nano-CeO_2/Zn–Mn composite conversion coatings on AZ91D magnesium alloy surface of corrosion resistance research, *Coatings*, 2023, **13**, 929.
31 M. Gobara, A. Baraka, R. Akid and M. Zorainy, Corrosion protection mechanism of Ce^{4+}/organic inhibitor for AA2024 in 3.5% NaCl, *RSC Adv.*, 2020, **10**, 2227–2240.
32 M. H. Mahmood, S. Suryanto, M. H. F. Al Hazza and F. I. Haidera, Developing of corrosion resistance nano copper oxide coating on copper using anodization in oxalate solution, *Int. J. Eng., Trans. B*, 2018, **31**, 450–455.
33 T. L. Nguyen, T. C. Cheng, J. Y. Yang, C. J. Pan and T. H. Lin, A zinc–manganese composite phosphate conversion coating for corrosion protection of AZ91D alloy: growth and characteristics, *J. Mater. Res. Technol.*, 2022, **19**, 2965–2980.
34 B. Djuričić and S. Pickering, Nanostructured cerium oxide: Preparation and properties of weakly-agglomerated powders, *J. Eur. Ceram. Soc.*, 1999, **19**, 1925–1934.
35 K. Castkova, A. Matousek, E. Bartonickova, J. Cihlar, P. Vanysek and J. Cihlar, Sintering of Ce, Sm, and Pr oxide nanorods, *J. Am. Ceram. Soc.*, 2016, **99**, 1155–1163.
36 A. Nefedova, K. Rausalu, E. Zusinaite, A. Vanetsev, M. Rosenberg, K. Koppel, S. Lilla, M. Visnapuu, K. Smits, V. Kisand, T. Tätte and A. Ivask, Antiviral efficacy of cerium oxide nanoparticles, *Sci. Rep.*, 2022, **12**, 1–16.
37 J. Calvache-Muñoz, F. A. Prado and J. E. Rodríguez-Páez, Cerium oxide nanoparticles: Synthesis, characterization and tentative mechanism of particle formation, *Colloids Surf., A*, 2017, **529**, 146–159.
38 J. Saranya, B. S. Sreeja, G. Padmalaya, S. Radha and T. Manikandan, Ultrasonic assisted cerium oxide/graphene oxide hybrid: Preparation, anti-proliferative, apoptotic induction and G2/M cell cycle arrest in HeLa cell lines, *J. Inorg. Organomet. Polym. Mater.*, 2020, **30**, 2666–2676.
39 L. Tan, Q. Tao, H. Gao, J. Li, D. Jia and M. Yang, Preparation and catalytic performance of mesoporous ceria-base composites CuO/CeO_2, Fe_2O_3/CeO_2 and La_2O_3/CeO_2, *J. Porous Mater.*, 2017, **24**, 795–803.
40 N. Rezaee, M. M. Attar and B. Ramezanzadeh, Studying corrosion performance, microstructure and adhesion properties of a room temperature zinc phosphate conversion coating containing Mn^{2+} on mild steel, *Surf. Coat. Technol.*, 2013, **236**, 361–367.
41 M. P. Rao, P. Sathishkumar, R. V. Mangalaraja, A. M. Asiri, P. Sivashanmugam and S. Anandan, Simple and low-cost synthesis of CuO nanosheets for visible-light-driven photocatalytic degradation of textile dyes, *J. Environ. Chem. Eng.*, 2018, **6**, 2003–2010.
42 R. Bortamuly, G. Konwar, P. K. Boruah, M. R. Das, D. Mahanta and P. Saikia, CeO_2-PANI-HCl and CeO_2-PANI-PTSA composites: synthesis, characterization, and utilization as supercapacitor electrode materials, *Ionics*, 2020, **26**, 5747–5756.
43 J. Gong, F. Meng, X. Yang, Z. Fan and H. Li, Controlled hydrothermal synthesis of triangular CeO_2 nanosheets and their formation mechanism and optical properties, *J. Alloys Compd.*, 2016, **689**, 606–616.
44 D. H. Youn, N. M. Tran, B. J. Kim, Y. Kim, J. P. Jeon and H. Yoo, Shape effect of cerium oxide nanoparticles on mild traumatic brain injury, *Sci. Rep.*, 2021, **11**, 1–8.
45 C. Wu, M. Yin, S. O. Brien and J. T. Koberstein, Quantitative analysis of copper oxide nanoparticle, *Chem. Mater.*, 2006, **18**, 6054–6058.
46 J. Mim, M. S. Sultana, P. K. Dhar, M. K. Hasan and S. K. Dutta, Green mediated synthesis of cerium oxide nanoparticles by using Oroxylum indicum for evaluation of catalytic and biomedical activity, *RSC Adv.*, 2024, **14**, 25409–25424.
47 A. Adhilakshmi, K. Ravichandran and T. S. N. Sankara Narayanan, Cathodic electrodeposition of zinc-zinc phosphate-calcium phosphate composite coatings on pure iron for biodegradable implant applications, *New J. Chem.*, 2020, **44**, 6475–6489.
48 R. Amini, H. Vakili and B. Ramezanzadeh, Studying the effects of poly (vinyl) alcohol on the morphology and anti-corrosion performance of phosphate coating applied on steel surface, *J. Taiwan Inst. Chem. Eng.*, 2016, **58**, 542–551.
49 R. Zeng, Z. Lan, L. Kong, Y. Huang and H. Cui, Characterization of calcium-modified zinc phosphate conversion coatings and their influences on corrosion resistance of AZ31 alloy, *Surf. Coat. Technol.*, 2011, **205**, 3347–3355.
50 S. Hu, Y. Fan, M. Muhammad, M. Wang, R. Ma, A. Du, X. Zhao and X. Cao, Corrosion resistance performance of nano-MoS_2-containing zinc phosphate coating on Q235 steel, *Mater. Lett.*, 2020, **265**, 6–9.
51 T. S. N. S. Narayanan, Surface pretreatment by phosphate conversion coatings – A review, *Rev. Adv. Mater. Sci.*, 2005, **9**, 130–177.
52 Y. Zhang and H. Wang, Novel phosphate conversion coating with superior corrosion resistance on the Mg-Al-RE alloy based on the introduction of silane, *ACS Omega*, 2023, **8**, 29374–29387.

53 B. P. Charitha and P. Rao, Pullulan as a potent green inhibitor for corrosion mitigation of aluminum composite: Electrochemical and surface studies, *Int. J. Biol. Macromol.*, 2018, **112**, 461–472.

54 G. Lou, P. Jia, X. Teng, J. Zhang, Z. Ye, H. Wu and J. Leng, Nano ZnO-assisted formation of zinc phosphate conversion coating for improving corrosion protection of AZ91D magnesium alloy, *Mater. Res. Express*, 2019, **6**, 086405.

55 J. Shang, S. Sun and S. Liu, Corrosion resistance and mechanism of (100), (110) and (111) preferred orientation of single crystal copper in NaCl solution, *Int. J. Electrochem. Sci.*, 2023, **18**, 100378.

56 Y. Tian, W. Li, Q. Yang, Y. Gong, W. Yue, Y. Ou, C. Li and X. Sheng, PDA@α-ZrP/SiO_2 incorporated phosphate coating with enhanced corrosion resistance and friction resistance, *RSC Adv.*, 2024, **14**, 24661–24670.

57 M. Akbari, B. S. Boroujeny and M. Raeissi, Cerium oxide nanoparticles as an accelerating agent for zinc phosphate coatings with enhanced corrosion resistance, *J. Adv. Mater. Process.*, 2021, **9**, 3–16.

58 X. Sun, D. Susac, R. Li, K. C. Wong, T. Foster and K. A. R. Mitchell, Some observations for effects of copper on zinc phosphate conversion coatings on aluminum surfaces, *Surf. Coat. Technol.*, 2002, **155**, 46–50.